LUNAR DIFFERENTIAL FLUX SCANS AT 22 MICRONS

LUNAR DIFFERENTIAL FLUX SCANS AT 22 MICRONS

Wendell W. Mendell

Space Science Departmen

Rice University

July, 1971

I. ABSTRACT

The nighttime lunar surface has been scanned at a variety of phases both before and after new Moon. A differential chopping technique was used which records the flux difference between adjacent resolution elements along a scan. In principle the differential scan can be integrated to provide the flux distribution, but slow drifts in the sensor null level frustrated this procedure. However, some cold limb temperatures have been calculated using the planet Jupiter for calibration.

The measurements were made with a resolution element of 27 arc seconds on the 28-inch telescope at the University of Arizona. Scan positions were determined by noting features on the illuminated portion of the Moon through a bore-sighted guide telescope. Positional accuracies are within two resolution elements. The technique is particularly sensitive to the detection of nighttime anomalies, and more than 150 of these have been identified.

Prior to new Moon is seen large scale thermal structure, corresponding to a previously unknown nonlinear cooling property of the lunar highlands. The nonlinear behavior consistently disappears 3.5 to 4 days after sunset. The effect could be due to the large scale roughness of the highlands or to a significant rock population with a mean size on the order of 10 cm.

2. ACKNOWLEDGEMENTS

I wish to acknowledge the contribution of my adviser, Dr. Frank Low, who conceived and initiated this project. His expertise in infrared astronomy is the pillar around which the effort was built.

My employer, the National Aeronautics and Space Administration, has been exceedingly cooperative in permitting me to undertake this project in conjunction with a degree program at Rice University.

My wife Bev has provided moral support during extended periods of frustration during which there seemed to be no reasonable solution to problems in the data.

This work was supported by the National Aeronsutics and Space Administration under Grant NGR 03-002-110.

3. TABLE OF CONTENTS

4. LIST OF FIGURES

5. LIST OF TABLES

6. INTRODUCTION

The Moon is the Earth's nearest celestial neighbor and, as such, has been the subject of astronomical investigation since the construction of Gallileo's telescope. Until the present day, Man has been bound to the Earth; and lunar studies have consisted of charting the Moon's motion through the sky, observing surface features, and measuring radiation reflected or emitted from the lunar surface.

Emitted infrared radiation from the Moon is directly related to the surface temperature through the Planck radiation function. A map of infrared radiance over the lunar disk can be converted to a map of temperatures after the spectral response of the detection system and the terrestrial atmosphere have been taken into account. The variation of surface temperature with time in response to the periodic solar heating is determined by the physical constants of the surface layer of the Moon. It is known from thermal studies that the affected surface layer is less than a meter thick.

The laws of physics allow the inference of the physical properties of this layer from a measurement of the surface temperature variation with time. Tracking the temperature of the lunar surface throughout the lunation cycle has thus far eluded observers due to the difficulty of detecting the very low temperatures on the dark Moon. As is often the case, the most difficult part of the measurement is also the most sensitive to variations in physical properties from point to point on the surface.

The work reported here is the "next step" in the field of lunar infrared observation. It occupies this place with respect to its objectives, its instrumentation, and its observational technique. The fact that the effort did not achieve all of its original goals implies (hopefully) that it is not the last step. This point will be revisited in the final section on recommendations.

7. INTERPRETATION OF LUNAR TEMPERATURES

In principle, the lunar thermal problem can be handled in a straightforward manner. The Sun is the only significant heat source, and the coupling between it and the airless lunar surface is entirely radiative The Moon's rotational equator and its orbital plane lie very nearly in the ecliptic so that the solar insolation represents a periodic boundary condition. The curvature of the lunar sphere is small enough that the solution to the one-dimensional heat equation for a semi-infinite slab can be utilized.

The one-dimensional heat equation can be written as

$$\rho c \frac{\partial T(z,t)}{\partial t} = \kappa \frac{\partial^2 T(z,t)}{\partial z^2} \qquad (1)$$

where t is the time variable, z is the distance into the surface, T is the temperature, κ is the thermal conductivity, ρ is the bulk density, and c is the specific heat. The physical parameters κ, ρ, and c are assumed to be constants in this first approximation. The solution to this equation for the lunar case was discussed first by Wesselink (1948).

The periodicity of the solar boundary condition implies that the surface temperature may be written as a Fourier series.

$$T(0,t) = \sum_{n=0}^{\infty} b_n \cos\left(\frac{2\pi n t}{P} + \phi_n\right) \qquad (2)$$

where P is the period of a lunation (29.53 days) and ϕ_n is a phase lag for the n^{th} harmonic. The solution for the temperature field in the semi-infinite slab with a sinusoidal surface temperature is well known (Carslaw and Jaeger, 1959). Equation (1) is first made dimensionless by defining the new variables,

$$\tau = \frac{t}{P} \; ; \; \xi = \frac{z}{\ell} \; ; \; \ell = 2\left(\frac{\pi P \kappa}{\rho c}\right)^{1/2} \qquad (3)$$

The solution to (1) with boundary condition (2) can then be written as

$$T(\xi,\tau) = \sum_{n=0}^{\infty} b_n \exp[-2\pi\xi\sqrt{n}] \cos 2\pi(n\tau - \xi\sqrt{n} + \phi_n) \qquad (4)$$

This sum represents a harmonic series of damped thermal waves. The wave length of an individual wave is $1/\sqrt{n}$ and the period is P/n. The damping is more severe for the higher harmonics. As $z \to \infty$, the temperature becomes constant ($T(\infty,\tau) = b_o$).

The problem can be viewed at this point as finding the b_n, the Fourier coefficients of the time expansion of the surface temperature. The relationship between the solar radiative input and the surface temperature is

$$(1-A)\,S(t) = \varepsilon\sigma T^4(0,t) - \kappa \frac{\partial T}{\partial z}\bigg|_{z=0} \qquad (5)$$

where S(t) is the incident solar flux, A is the albedo of the surface for solar radiation, and ε is the emissivity of the surface at the infrared wavelengths corresponding to planetary thermal emission. Using equations (3), the dimensionless form of (5) is

$$(1-A)\,S(\tau) = \varepsilon\sigma T^4(0,\tau) - \frac{1}{\Gamma\sqrt{4\pi P}} \frac{\partial T}{\partial \xi}\bigg|_{\xi=0}, \qquad (6)$$

where $\gamma = (\kappa\rho c)^{-1/2}$

The variation of solar flux with time is the product of two functions. Changes in the solar constant with the Sun-Moon distance are usually ignored. The remaining variation is the change in sun angle relative to the local normal as a result of the Moon's rotation. Under the approximation that the Sun stays in the Moon's equatorial plane, the flux impinging upon a surface element at latitude β as a function of time is

$$\begin{aligned} S(\tau) &= S_o \cos\beta \cos 2\pi\tau \qquad \text{for } 0 \le \tau \le \tfrac{1}{4} \text{ and } \tfrac{3}{4} \le \tau \le 1 \\ &= 0 \qquad\qquad\qquad\quad \text{for } \tfrac{1}{4} \le \tau \le \tfrac{3}{4}, \end{aligned} \qquad (7)$$

where S_o is the solar constant. The point $\tau = 0$ corresponds to local noon.

It is easy to see that the substitution of (4) into (6) results in a set of coupled equations for the b_n due to the presence of the quadratic temperature term. The resultant non-linear set of equations cannot be solved analytically; the original heat equation must be integrated numerically. Fortunately, this is possible using a simple finite difference technique as explained by Wesselink (1948).

An examination of (6) shows that the only lunar parameters are A, ε, and γ. The solar albedo of a surface region can be determined from lunar photometric measurements, and the infrared emissivity is very nearly unity. Thus for practical purposes the lunar thermal problem becomes one of finding the proper value of γ to characterize an area.

Figure 1 shows a family of lunation curves calculated for various values of γ (Krotikov and Shchuko, 1963). The value $\gamma = 20$ corresponds to the thermal properties of rock. For higher values of the parameter which are typical of the lunar surface, it is important to note that the curves are indistinguishable during the lunar day. While the Sun is above the horizon, the surface temperature is determined by the local albedo and slope. It is the nighttime temperature which defines the proper value of the thermal parameter.

A similar analysis may be performed for the case of a lunar eclipse. The difference lies in the fact that the insolation function is not periodic but depends on the size and path of the Earth's shadow. The solution is again obtained through numerical integration of the heat equation. However, the initial temperature distribution is important and is obtained by a solution of the lunation case. Once again the

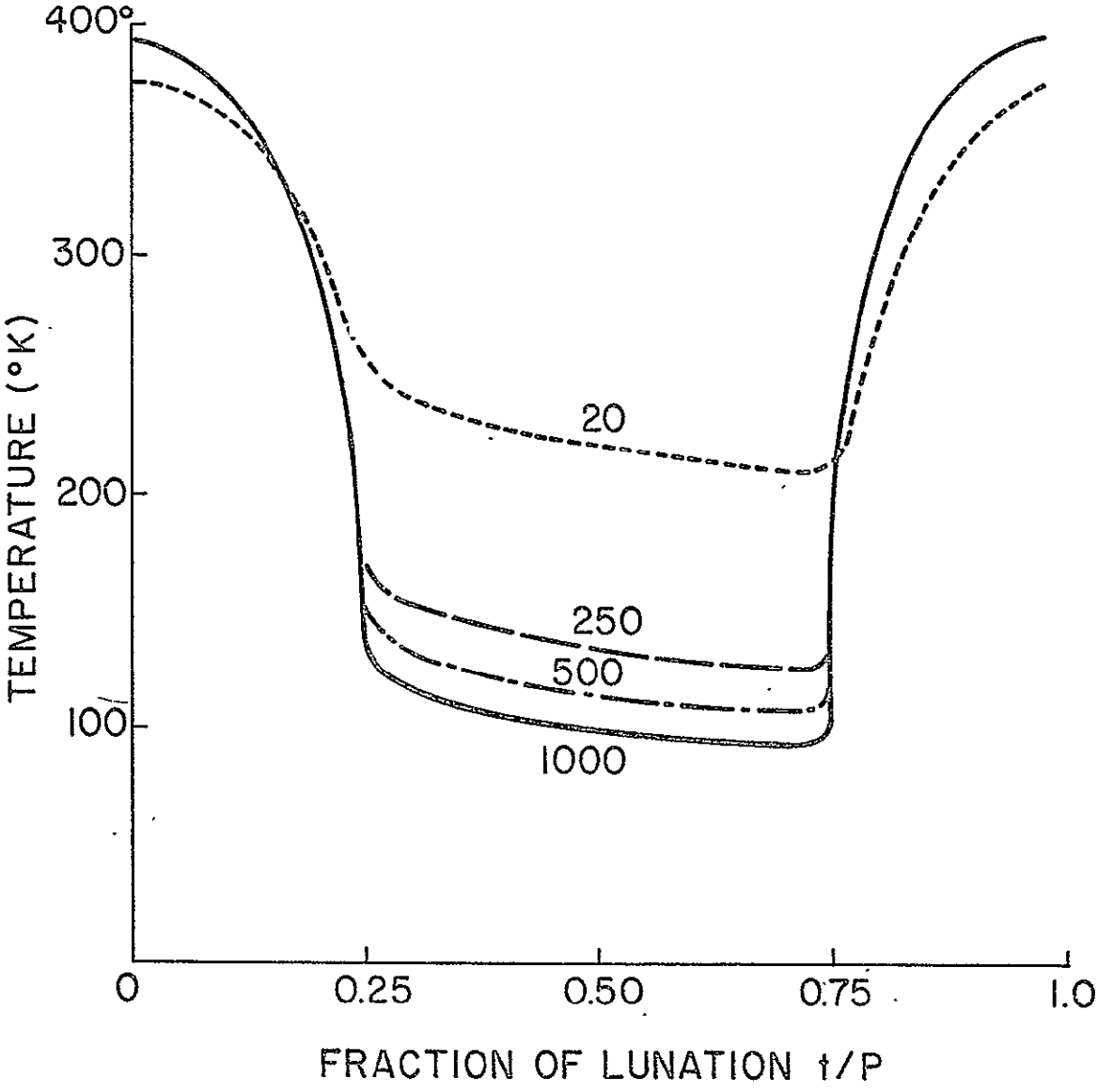

FIGURE I. CALCULATED LUNATION TEMPERATURES FOR VARIOUS VALUES OF $(\kappa pc)^{-1/2}$ FROM KROTIKOV AND SHCHUKO, 1963.

family of solutions has γ as a single parameter characterizing the thermal properties of the lunar surface.

The homogenous, or single parameter, model of the lunar surface has been under fire since its inception for various shortcomings. The earliest and most persistent objections came from radio astronomers who were unable to reconcile their results with the theory (Piddington and Minnett, 1949). Jaeger and Harper (1950) developed a layered model which appeared to resolve the conflict. Closer theoretical analysis of the observational problem (Weaver, 1964) reveals that the radio astronomy evidence against the homogenous model is far from convincing due to the difficulty of deconvoluting the lunar temperature distribution from the low resolution antenna pattern.

The most embarassing deficiency of the homogenous model is the discrepancy between the values of γ derived from eclipse and lunation observations. Linsky (1966) points out that both Wesselink (1948) and Jaeger (1953) fit Pettit's (1940) eclipse measurements with $\gamma \geq 1000$, while the lunar midnight temperature of approximately $120^{\circ}K$ as measured by Pettit and Nicholson (1930) and Sinton (1959) is consistent with $\gamma \simeq 500$. Winter and Saari (1969) reiterate the argument with more modern data, fitting the lunation and eclipse situations with γ's of 800 and 1300, respectively.

A recent measurement of the lunar midnight temperature by Mendell and Low (1970) yielded a value of $101^{\circ}K$, corresponding to $\gamma \simeq 875$. A reassessment of Pettit's data, based on a more accurate value of the pre-eclipse temperature, gives a value of $\gamma \leq 1000$. Thus the disagreement

in the older data is not so severe, but the analysis by Winter and Saari establishes the inadequacy of the homogenous model and demonstrates the success of their semi-empirical particulate model incorporating radiative transfer.

8. HISTORY OF LUNAR INFRARED MEASUREMENTS

The objectives and techniques associated with the work reported here are best viewed in their historical context. Most early work centered around dayside and eclipse measurements because they were convenient and straightforward. The analysis from the previous section shows that the eclipse data was the more important. Lunar nighttime measurements are more important still, but they have required improvement in the observational technique.

The year 1960 has been taken as the beginning of "modern" infrared observation in the following review. After that year cryogenic detectors became available and greatly improved the achievable spatial resolution and noise equivalent temperature. In addition it was discovered that individual features displayed distinctive thermal signatures during an eclipse. The search then began to verify the existence of "thermal anomalies" during the lunar night.

a. Early Work

The first infrared measurements of the Moon were published by the Earl of Rosse in 1869. He used a thermocouple in the focal plane of his telescope to detect the radiation from the lunar disk. His value for the full Moon temperature was too high due to lack of knowledge regarding the transmission of the Earth's atmosphere.

Extensive study of the Moon's thermal emission was carried out by Pettit and Nicholson (1930). They determined the distribution of radiation over the lunar disk at full moon, the apparent temperature of the subsolar

point as a function of phase angle, the temperature history of a poin during an eclipse, and the lunar midnight temperature. Pettit followed this work with measurement of integrated emission over the disk as a function of phase (1935) and further eclipse measurements (1940). This body of data became the prime reference work for lunar surface thermal models for over a quarter of a century.

Unfortunately the results from this work were quantitatively erroneous although qualitatively correct. The inaccuracies originated in a calibration error (Pettit, 1945), an improper integration of the radiant flux over angles (Ashby, 1966), and incomplete knowledge of the transmission of the atmosphere and their rock salt filter (Saari, 1964). Their published subsolar point temperature of 374^{O}K was too low, and their antisolar point temperature was too high. These errors affected not only the theoreticians and their models but also significant bodies of experimental data. Pettit's eclipse temperatures (1940) were based on the subsolar point determination, and most of the Russian radio telescope measurements were carefully tailored to be consistent with the Pettit and Nicholson values via Troitskii's original analysis (1954). In the late Sixties papers were still being written based on this data, either directly or indirectly.

After the Second World War radio astronomers, particularly the Soviets, began measurement of lunar temperatures when Dicke and Behringer (1946) demonstrated the feasibility of the technique. Using optical techniques, Sinton measured surface emission during a lunation (1955) and an eclipse (1956) at a wavelength of 1.5 mm. His telescope was a modified searchlight mirror with a Golay cell at the primary focus. He demonstrated

that the phase lag associated with long wavelength temperatures, already demonstrated for a lunation (Piddington and Minnett, 1949), also occurred during an eclipse.

Infrared detection of the Moon was resumed by Sinton with the construction of a new pyrometer detector (1959). The instrument measured the difference in energy passing through two apertures in the focal plane of the telescope. This technique is designed to cancel out sky radiation. In practice, a planetary area fills one aperture while the second aperture looks at an adjacent patch of sky. The device embodies two Golay cell detectors, and a chopper wheel alternately imaged the apertures onto the detectors. In other words, in the first half of the chopping cycle the first aperture was imaged on the first detector and the second aperture was imaged onto the second detector; for the second half of the chopping cycle, the reverse was the case. The wavelength band was determined by a removable array of restrahlen mirrors as well as a transmission filter. For measurements of extended sources such as the Moon, one aperture was closed off.

At a wavelength of 11.9 microns, Sinton (1959) measured the antisolar temperature of the Moon to be $122^{\circ}K \pm 3^{\circ}K$, in agreement with the results of Pettit and Nicholson (1930). The reason for the error in this measurement is not known (Saari, 1964).

Using Sinton's pyrometer with the 8.8 micron filter arrangement, Geoffrion, et al (1960), also mapped the illuminated portion of the Moon at various phases. The telescope was clamped in hour angle and declination, and the Moon's motion in the sky caused it to drift past

the detector. The telescope was then moved to another hour angle, and the process was repeated. The declination of the detector was always maintained so that the Moon's own motion in declination provided spacing between the scans. From the matrix of data points thus generated, isotherms were constructed for the illuminated portion of the Moon. The thermal contours were shown to be approximately concentric about the subsolar point although there was some variation from this structure due to mare-highland thermal differences. The apparent emission from the subsolar point was seen to fall off toward the limb. This surface roughness effect was also observed by Pettit and Nicholson. Sinton's plot of subsolar point emission versus phase angle has essentially the same shape as that of the earlier work, but the measured value of the emission is consistently less. A subsolar point temperature was determined as 389°K.

At this point in time (circa 1960), one of the experimental facts known about the Moon was the homogeneity of optical reflectance properties everywhere over the visible disk (cf. review paper by Pearse, 1963). Except for some apparent thermal enhancement of the maria detected by Sinton (see above), this startling uniformity of surface properties over a wide range of surface morphology was also seen in thermal data. The discovery of thermally enhanced areas during an eclipse lent a new vitality to lunar infrared measurements.

b. Modern Eclipse Measurements

Shorthill, et al (1960) used a thermistor bolometer at the Newtonian focus of a 72-inch reflecting telescope to detect the Moon's thermal

emission during the eclipse of March 12-13, 1960. The detector sensitivity corresponded to a temperature difference of 20°K on a background temperature of 180°K. Temporary cloudiness permitted measurements only after the onset of totality. Scans were made across the disk by driving the telescope in right ascension. Particular care was taken to scan across several prominent lunar craters. Associated with Tycho was a deflection as high as three times the background, corresponding to a temperature enhancement of 50°K. Other craters scanned included Aristarchus, Copernicus, Eratosthenes, and Alphonsus; but only the first two showed enhancement in subsequent analysis of the data.

Sinton (1962) used his pyrometer to monitor the temperature of Tycho and its environs during part of the eclipse of September 5, 1960. The data points have a fair amount of scatter during the beginning of the umbral phase. Using curves previously calculated by Jaeger and Harper (1950), Sinton concludes that the observations are consistent with a two-layer thermal model having a surficial dust layer 0.3 mm. thick. Of 17 ray craters observed during an eclipse, all but Proclus were anomalously warm.

Shorthill and Saari also took advantage of the September 5 eclipse to make raster scans over limited areas of the lunar surface (Shorthill and Saari, 1961; Shorthill, 1962; Saari and Shorthill, 1962). Several prominent craters were studied using a thermistor bolometer at the Newtonian focus of the 60-inch Mount Wilson telescope. Sensor resolution was 8 seconds of arc (15 kilometers at the center of the disk). The scanning technique consisted of tracking the Moon with the telescope drive near the lunar rate and then moving the telescope alternately

east and west with the right ascension setting motion. The Moon's own drift in declination caused the scan lines to form a sawtooth pattern on the lunar surface, thereby traversing the area of interest. Measurements were made on the illuminated Moon on the days just before and after the eclipse as well as on the night of the eclipse itself, preceding the penumbral phase. Scanning continued on into the eclipse, partially into the onset of totality, at which time the Moon was positioned too low in the sky to proceed.

A great deal of thermal structure was found in the isothermal contour maps constructed from the scan data. Thermal differences on th illuminated Moon could generally be explained by local geometry and/or albedo variations.

During the eclipse, scans were made over Aristarchus, Copernicus, Kepler, Proclus, and Tycho. All were found to be thermal anomalies, i.e. warmer than their environs during the umbral phase of the eclipse. In addition, measurements on the first three showed that they were cooler than their environs in the early stages of the eclipse. For Aristarchus the crossover point of equal temperature occurred approximately 20% of the way through the penumbral stage. After approximately 80% of the penumbral phase, the ratio of the enchanced radiance from Aristarchus to that of its environs reached a value which it maintained until measurements ceased during totality.

The authors made an approximate calculation of the energy balance of Menelaus, Copernicus, Aristarchus and their environs under solar illumination by considering their measured visible albedo and reflecting properties and by neglecting conduction into the interior. The

predicted temperature differences were invariably lower than observed. They concluded that either the integrated solar albedo differed from the visible albedo or that conduction into the surface is not negligible for the rayed craters. The former is now known to be true (Wattson and Danielson, 1965; Adams and Jones, 1970). Integrated solar albedos have not been determined for individual areas on the Moon, and it is difficult to estimate them from the general lunar curve due to widespread color variations on the Moon (McCord, 1969). At this point it is difficult to say whether subsurface conduction is important in explaining the depressed temperature of rayed craters on the illuminated Moon.

A study of the cooling curves of four rayed craters during the eclipse revealed that emissivity variations could account for the temperature differences only if these variations were unreasonably large. Attempts to fit the data to two-layer conduction models gave dust layers only fractions of a millimeter thick. It is questionable whether the model has any physical significance for such thin layers.

Beginning in 1963, Shorthill and Saari undertook the ambitious project of mapping the illuminated Moon in both the visible and the thermal infrared throughout an entire lunation. To augment this work, they also mapped the entire disk several times during the eclipse of December 19, 1964. These significant contributions to the body of lunar information were made possible by the use of a mercury-doped germanium detector cooled to liquid neon temperatures in a focal plane scanner. Utilizing the sensitivity of the semiconductor detector, they could scan the whole lunar disk during totality of the eclipse in less than half an hour.

Although the collection of dayside measurements (Saari and Shorthill, 1967) represents an important compendium of lunar data, the really exciting results lie in the eclipse work. The survey of the shadowed lunar disk revealed approximately 1000 thermal anomalies at the resolution of the sensor (10 seconds of arc). In addition there were extended regions of thermal enhancement (e.g. Mare Humorum in its entirety). The distribution of the anomalies was decidedly non-random, with the maria having more than the highlands. Inhomogeneity in the distribution can be explained by local properties prolonging and enhancing thermal behavior (Shorthill and Saari, 1965).

The overwhelming majority of the anomalies are associated with visually bright craters, and most of the remainder can be correlated with rilles or areas which are bright at full moon. On the other hand, not all bright features are thermally anomalous. The enhancement attributed to Mösting C, corrected for the fact that the crater is smaller than the sensor, can be explained with thermal parameters of bare rock. It might be anticipated that such a feature would exhibit a strong radar return, and there is some correlation between radar and thermal enhancement of lunar features. However the relationship is not straightforward. For example, the uplands have a higher radar reflectivity whereas the maria are more thermally active.

c. Modern Lunation Measurements

The discovery of thermal inhomogeneity on the lunar surface during an eclipse lent impetus to the measurement of temperatures on the

unilluminated portion of the Moon during a lunation. Whereas an eclipse lasts for only a few hours, the lunar night has a duration of more than fourteen days. During the night thermal contrasts are heightened. The surface temperature is affected by the heat flow from greater depths due to the prolonged absence of insolation. On the other hand, nighttime temperatures are lower than eclipse temperatures and therefore more difficult to detect.

With the advent of the cryogenically cooled, doped semiconductor detectors it became possible to sense the low-temperature radiation from the night side of the Moon's sunset terminator. Even with these detectors the signal generally fell below the system noise level before the anti-solar meridian was reached. The impossibility of rapid nighttime scanning due to low signal levels and the optical invisibility of the unilluminated Moon together compound the observational problem of measuring cooling curves of specific features. The observational approach has been to scan across the sunset terminator until the signal disappears into the noise and then to treat the scan as equivalent to a portion of a lunar cooling curve.

Murray and Wildey (1964) used a mercury-doped germanium photoconductor cooled to liquid hydrogen temperature in a 19-inch telescope at White Mountain, California. The spectral bandpass of the system was 8 to 14 microns, and the spatial resolution was 17 seconds of arc. The dual-beam photometer alternately imaged the Moon and the sky onto the detector 180 Hz by means of a chopper wheel. The signal to noise ratio became approximately one at a scene brightness temperature of 105°K.

The telescope was directed at a feature on the illuminated portion of the Moon and driven in right ascension onto the dark portion until the signal disappeared into the sky noise. The drive was then reversed, and the sensor was moved back onto the illuminated portion. The Moon's motion in declination prevented superposition of the two halves of the scan. Positional information was derived from photogrpahy taken before, after, and occasionally during each scan. Positional error was estimated to be no more than two or three times a resolution element although undetected systematic offsets could make this number five times the resolution in isolated cases.

Most scans displayed a sharp gradient after nightfall followed by an abrupt change in the temperature range 120°K to 145°K to a gentler slope, the latter continuing until the system noise level was reached by the signal. In the analysis of the data, anomalous areas were definitely identified around Copernicus and Tycho; and suspected groupings of anomalies were seen along some mare borders. The enhancements associated with each of the two rayed craters consisted of a complex of anomalies rather than just the single anomaly of the crater itself. There appeared to be structure smaller than the photometer resolution. A search for Tycho was made 10 or 12 days into the lunar nighttime when the Moon was near first quarter, but the crater was unobservable.

Murray and Wildey averaged the two halves of one scan and compared this "cooling curve" to various homogenous models. They justified the comparison by the observation that thermal differences due to mare-upland physiography and albedo quickly disappeared after nightfall on the Moon.

The fit between theory and observation was very poor. They concluded that conductive material must be intermixed with lunar soil at or very near to surface.

An almost identical measurement was performed by Shorthill and Saari (1965). The spatial resolution was 8 seconds of arc and the passband of the system was 10 to 12 microns; but otherwise the technique and instrumentation were very similar. However, cooling curves from this effort and the one cited above, constructed from scans over approximately the same region, disagreed significantly as to shape. The reason for the difference is not clear. Possible explanations include differences in the scan paths and variations in the sky emission or the lunar surface emissivity associated with the differences in the spectral passbands of the experimental setups.

Wildey, et al (1967) mapped a portion of the post-sunset nighttime surface in an extension of the earlier work by Murray and Wildey. The experimental setup was very similar except that the spatial resolution was approximately 23 seconds of arc, somewhat lower than before. The minimum detectable surface brightness corresponded to approximately 100°K. In this paper and a later one (Wildey, 1968) over 100 post-sunset nighttime anomalies were documented. Low level enhanced emission was observed from some maria.

Low (1964) established an upper limit of 100°K in the cold limb temperature of the unilluminated Moon using a gallium-doped germanium bolometer (Low, 1961) in the 8 to 14 micron atmospheric window. The measurement was made using a differential observing technique. This technique increased the sensitivity of the measurement by monitoring the difference signal from two adjacent telescopic resolution elements,

thereby comparing (and effectively canceling) the thermal emission from practically the same column of atmosphere. This observational method will be discussed more thoroughly later in this paper.

Observing through the atmospheric window from 17.5 to 22 microns, Low (1965) established a mean cold limb temperature of $90^{\circ}K$. This measurement confirmed Wesselink's predicted temperatures using $\gamma=1000$ $cm^2 deg\ cal^{-1}\ sec^{-1/2}$. However the cold limb temperature varied considerably about the mean, suggesting a corresponding variation of lunar thermal properties. The coldest areas observed had temperatures $\leq 70^{\circ}K$, implying that $\gamma \geq 2300$ $cm^2 deg\ cal^{-1}\ sec^{-1/2}$. Such areas represent "cold anomalies" in that for explanation of their thermal properties one must return to the supposedly outmoded concept of a thick dust layer.

Low also detected a very hot spot on the southeastern limb of the Moon. This source was subsequently found again and determined to be the crater Tycho (Low and Mendell, 1968). Its temperature was determined as $147^{\circ}K \pm 18^{\circ}K$ when it was located approximately 13 days into the lunar night. Allen and Ney (1969) measured the brightness temperature of Tycho at 12 microns to be approximately $140^{\circ}K$. However an infrared spectrum of Tycho in the 8 - 14 micron region revealed a color temperature of $200^{\circ}K$.

9. PRIOR OBSERVATIONAL TECHNIQUES

The astronomer, whether visible or infrared, is always confronted by a series of observational problems due to the Earth's atmosphere. For the astronomer interested in the "thermal" infrared, the atmosphere not only absorbs radiation from the object of interest but also emits its own thermal radiation in equal proportion. This atmospheric emission constitutes a ubiquitous background against which the signal must be discriminated. The magnitude of the background is a rather sensitive function of the observational circumstances, including the concentrations of the offending gases (mostly water, carbon dioxide, and ozone), the ambient temperature, the ambient pressure, and the path length through the atmosphere. The background is minimized for observations taken at the zenith from a high altitude under cold, dry, clear conditions. Degradation of image quality from atmospheric effects is a somewhat secondary consideration for infrared astronomy since the diffraction-limited performance of telescopes at these longer wavelengths is more than an order of magnitude worse than that at optical wavelengths.

The atmosphere is optically thick over most of the infrared region. Only a few atmospheric "windows" exhibit a sufficiently high transparency (and consequently low emission) to allow observation of extraterrestrial sources. The overwhelming majority of lunar observations have been made in the rather good window located between 8 and 14 microns. Only Frank Low has been able to exploit the potential of a second, less well defined window in the region of 17.5 to 25 microns. He was able to do this through a combination of detector technology and observing technique.

Exploration of an extended source such as the Moon requires a map, i.e. an infrared photograph. Since no suitable imaging devices exist for the thermal infrared, the map must be built up from a raster of scans across the Moon with the detector. The Moon must be tracked by the telescope during the scanning process, and the time required to complete the task should be as short as possible. Detector speeds are directly related to the required sensitivity, and this interrelationship begins to be a problem during mapping of an eclipse. The point is beautifully made by Shorthill and Saari (1965):

"In our previous work using a thermistor bolometer, the speed of scanning was limited by cell noise and sky background fluctuations to about six seconds of arc per second of time, which gave a minimum detectable temperature of 190°K. With this system it would have taken approximately 25 hours to scan the entire disk with eight seconds of arc spatial resolution.

"The present system uses an infrared mercury-doped germanium detector cooled to liquid hydrogen temperature. The reduction of cell noise over the thermistor detector is several orders of magnitude so that the scanning speed could be increased to 530 seconds of arc per second of time. A narrow bandpass filter from 10 to 12 microns rejected most of the sky emission."

A simple calculation shows that the scanning time of 25 hours with the old system drops to 17 minutes with the new one.

In their dark side measurements with a system time constant of approximately one second, Shorthill and Saari found a minimum detectable

temperature on the order of 105°K to 110°K. The limiting noise signal was apparently due to sky fluctuations because the signal smoothed out when the telescope was slewed rapidly across the sky in right ascension. Their system was single beam, in which the signal from the Moon or the sky was compared against a reference blackbody via a chopper wheel arrangement. In other words, no attempt was made to reduce the effect of sky emission during the measurement.

Murray and Wildey (1964) used a mercury-doped germanium detector in a double beam photometer for their darkside work. The lunar signal was chopped against a portion of the sky adjacent to the Moon using a chopper wheel. Their noise signal also limited the lowest detectable temperature to 105°K. The noise itself was due to "low-frequency" fluctuations with periods in the 10 - 100 second range, which the investigators attributed to non-stationary emission from the atmosphere, the telescope, and possibly the instrument itself.

Since the lowest temperature attainable on both systems was the same, it might appear that the sky cancellation approach was unprofitable Differences in the experimental setups belie this conclusion. Murray and Wildey used a much smaller telescope (24 inch versus 60 inch), which would exhibit a shorter time constant for background radiation. Their filter passed radiation from 8 to 14 microns, thus admitting sky emission from the wings of atmospheric absorption bands on either side of the window as well as the ozone emission in the window. However, there should be a major noise source due to the design of the instrument. The lunar signal reaches the detector via a reflection from a chopper blade.

The sky comparison signal reflects off of a stationary mirror and through a gap between chopper blades on alternate cycles. If the emittance of the chopper blades and the mirror are as high as 4% (Murray speculates it could be 7%), and if they are at room temperature (300°K), then an excursion of $\pm$ 0.1°K for each of them could provide a noise signal equal to a 105°K blackbody signal. This calculation demonstrates the importance of maintaining the same optical elements in the two beam paths.

When observing low temperature sources, it is also important to choose the proper atmospheric window. For low temperatures, the 8 to 14 micron window lies on the short wavelength side of the blackbody curve; and the available flux falls dramatically with decreasing temperature. There is 22 times as much flux from a 100°K blackbody available at 22 microns than there is at 11 microns; for an 80°K blackbody the ratio is 110. The investigators discussed here were unable to make use of the window at longer wavelengths because the mercury-doped germanium detector is a photoconductor with a long wavelength cutoff at 14 microns. The Low germanium bolometer is a thermal detector with no such wave length restriction.

From the above discussion it is clear that the dark Moon is best observed in the window at 20 microns using a sky cancellation technique which employs the same optical elements in both beams. Such a system was used in this work.

10. CURRENT INSTRUMENTATION AND TECHNIQUE

The observations described herein were taken on the 28-inch telescope of the University of Arizona in the Catalina Mountains outside Tucson. A helium-cooled, doped-germanium bolometer developed by Frank Low (1961) was mounted at the Cassegrain focus of the telescope. Sensor resolution was 27 seconds of arc. An interference filter with a spectral bandwidth of 17 to 25 microns and an effective wavelength of 22 microns was placed in front of the detector. The tracking motion of the telescope was set at the lunar rate; a raster scanning motion was superimposed upon the tracking motion. The location of the sensor element on the Moon was determined by means of a bore-sighted guide telescope.

The incoming beam of radiation was reflected off of the optical axis through a right angle into the detector by a small folding mirror. The folding mirror was driven in an oscillatory motion toward and away from the detector, perpendicular to the incoming beam. Figure 2 is a schematic representation of this assembly. The detector sequentially viewed a pair of adjacent resolution elements in the sky, alternating between the two at a rate of 10 Hz. The electronics in the radiometer subtracted the detector outputs due to the two beams and amplified only the difference. This system achieves the sky cancellation inherent in the dual beam approach but uses identical optical elements in both beams. The placement of the two beams contiguous to one another leads to maximum cancellation of sky emission and excellent sensitivity. A dual beam chopper using a wobbling mirror has been discussed by Low (1966).

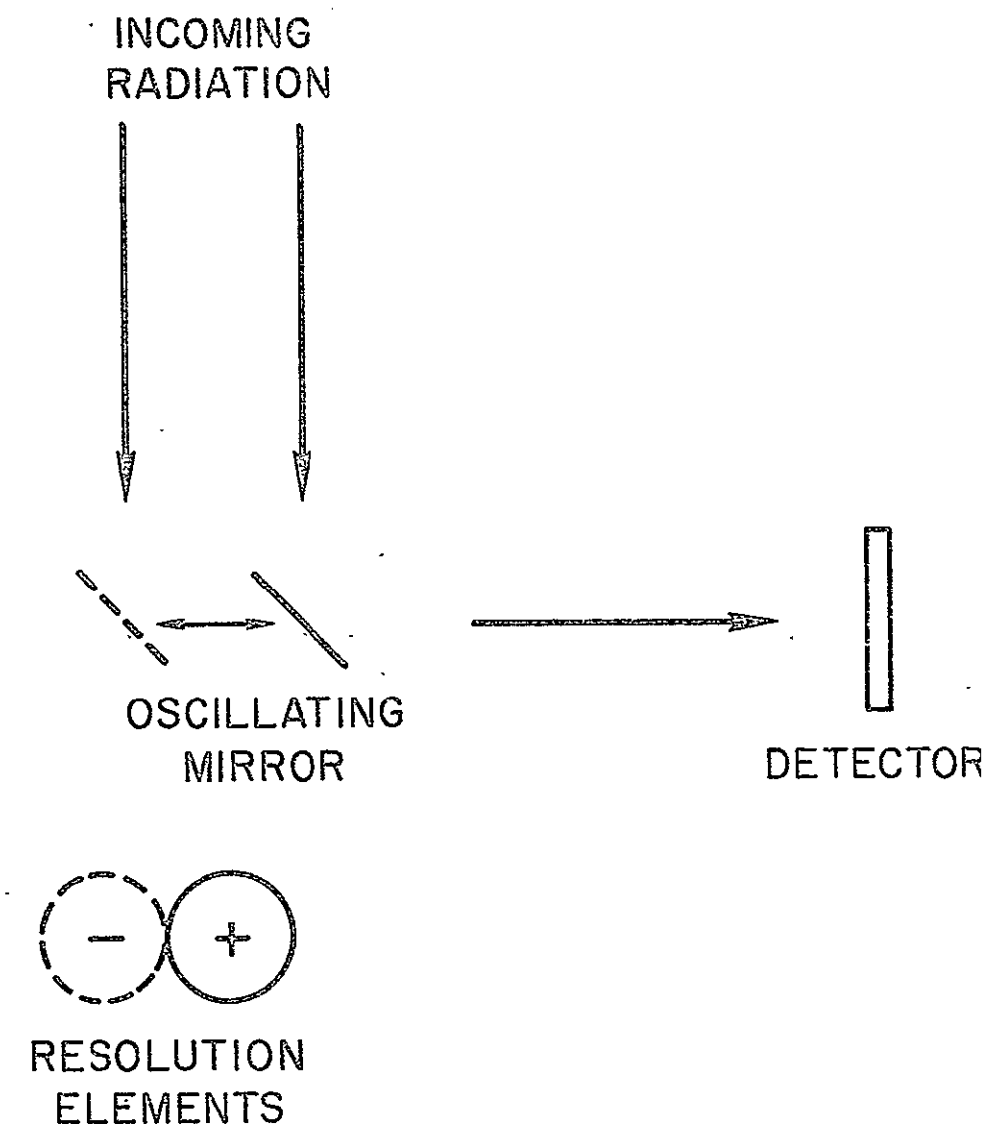

FIGURE 2. SCHEMATIC REPRESENTATION OF DUAL BEAM, DIFFERENTIAL SCANNING SYSTEM.

The mirror oscillation was oriented relative to the raster motion of the telescope such that the two beams always fell along a scan line. This is important so that the output can be interpreted as a differential measurement of the radiant flux distribution across the disk. In theory, the trace could be integrated to recover the actual flux distribution. Experimental difficulties generally prevented recovery of this information, except in special cases.

Figure 3 demonstrates the response of a differential system to three common situations. Limb deflections are excellent examples of edge crossings. Lunar anomalies are recognizable from the S-curve of the point source. Linear gradients, although common, were very difficult to detect because of drifts in the null level of the signal as discussed below. Isolated edges and point sources are easily picked out, but combinations of the three types of signal in Figure 3 are difficult to unravel due to uncertainties in instrumental effects.

The ac signal from the detector was amplified and then synchronously demodulated via a phase reference from the oscillating mirror. This signal was processed by a dc amplifier. The output could be used to run a chart recorder or could be fed through a voltage to frequency converter and digitized. A paper tape punch was the digital output device.

Data was degraded by problems with the processing and recording equipment. The paper tape punch performed erratically, but most of the data was recovered through time-consuming hand processing. Drift in the dc amplifier was a more subtle effect but ultimately limited our ability to integrate the scans. The effect of the drift was to cause

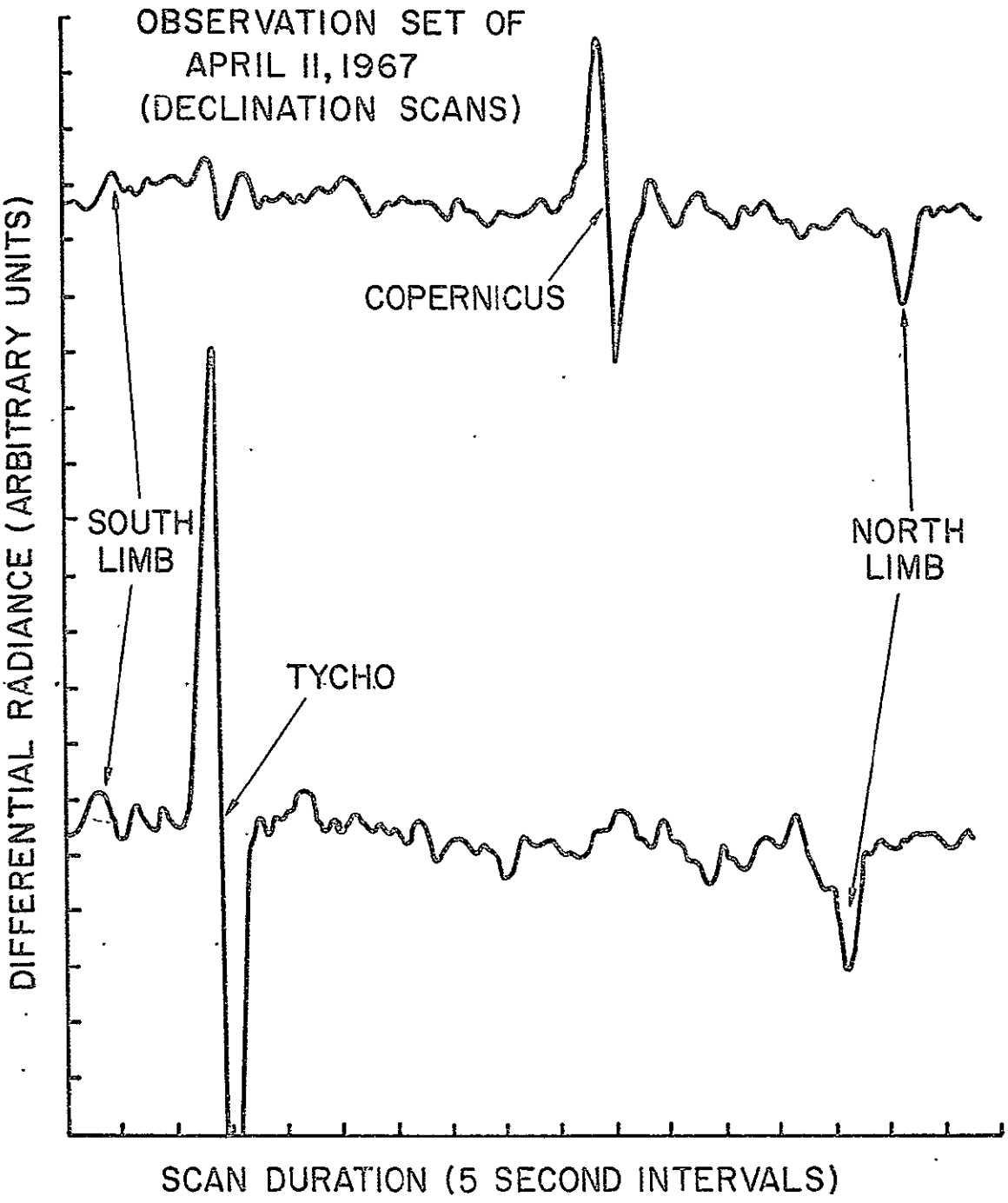

FIGURE 3. DECLINATION SCANS COMPARING DEFLECTIONS DUE TO COPERNICUS AND TYCHO ON THE NIGHTTIME MOON. COPERNICUS HAS BEEN UNILLUMINATED FOR 7.8 DAYS AND TYCHO FOR 8.5 DAYS.

the sky level reference to vary over a scan. In this manner spurious temperature gradients are introduced into the integrated scan. Scan integration often led to negative fluxes, a physical impossibility. Adjacent scans showed little correlation after integration.

Mapping of the unilluminated Moon is a difficult problem from an observational standpoint. Data is taken near new Moon, a daytime object. The interesting portion of the disk is essentially invisible to the observer. All selenographic reference points must be taken in the illuminated crescent. The signal from the lit portion saturated our system, and no correlation between the visual identification and the infrared scan could be made.

Automated tracking of the Moon through the sky is difficult since its motion is considerably more complex than that of other astronomical objects. Shorthill and Saari were able to map an eclipse because the scanning could be done quickly in the focal plane of the telescope. The motion of the telescope itself was confined to tracking alone and could be continuously monitored. The signal levels for darkside work are so low that the telescope must be used for both tracking and scanning. Any motion of the detector relative to the telescope would change the detector background sufficiently to overwhelm the lunar signal.

Initially we used a raster consisting of scan lines in declination spaced by steps in right ascension in a rectilinear pattern. The scan lines were roughly parallel to the terminator, and the pattern efficiently covered the dark portion of the disk. In this technique identification of anomalies depends critically on the stability of the raster relative

to the lunar disk. Reduction of the data revealed that the tracking was poor. Lack of timing marks and frequent adjustments of the scan rate by the observer frustrated attempts to correct for the drift.

The magnitude of the observational problems was not appreciated until after the completion of a set of observations in the summer of 1967. After a review of the problem, we decided to try to live with the residual drifts and monitor them by enlarging the scan pattern enough to contain drifts. Extremely poor observing conditions in the autumn and winter of 1967 limited us to only two days of observation with this method in December and January.

Beginning in February, 1968, all data was taken with scan lines in right ascension. This scheme has the advantage that a visual sighting from the illuminated crescent can be made on each scan. Conversely, the duty cycle of the detector in the area of interest is reduced. Reduction of the data revealed that the recorded landmarks were unreliable. It is possible that cumulative solar effects and winds upset the alignment of the telescopes over long observing sessions.

The differential observing technique is particularly suited for the detection of anomalies. Most of the data reduction effort concentrated on the identification of these features. Prominent nighttime anomalies were used as backups to the recorded visual scan locations. The eclipse thermal maps of Shorthill and Saari (1969) were particularly helpful in this aspect of the work.

II. DATA REDUCTION

a. Sensor Location

The key to the data reduction consists of deriving the transformations between selenographic coordinates and a set of coordinates related to the lunar disk as seen by the observer. The selenographic system has the z-direction pointing along the lunar rotational axis and the x-direction along a "mean" Earth-Moon line of centers. Observationally, it is more convenient to think of the lunar disk as a planar object projected onto the celestial sphere. To achieve this projection, an instantaneous z-axis lies along the Moon-observer line and the y-axis points northward in the plane of the declination circle containing the disk center. The American Ephemeris and Nautical Almanac contains the relevant transformation parameters between those two systems in the section on the physical observations of the Moon.

The telescope operates in a topocentric system of right ascension (α) and declination (δ), and it is important to relate this system to the usual observational system. At some time, t, let the geocentric equatorial coordinates of a lunar feature by (α,δ) and those of the center of the Moon be $(\alpha_{\mathbb{D}},\delta_{\mathbb{D}})$. For the time being we will neglect atmospheric refraction. We can define the following vectors (cf. Figure 4)

$\underline{\rho} = (\rho\cos\alpha\cos\delta, \rho\sin\alpha\cos\delta, \rho\sin\delta)$ - the vector from the point of observation to the lunar feature

$\underline{R} = (R\cos\alpha_{\mathbb{D}}\cos\delta_{\mathbb{D}}, R\sin\alpha_{\mathbb{D}}\cos\delta_{\mathbb{D}}, R\sin\delta_{\mathbb{D}})$ - vector from the point of observation to the center of the Moon;

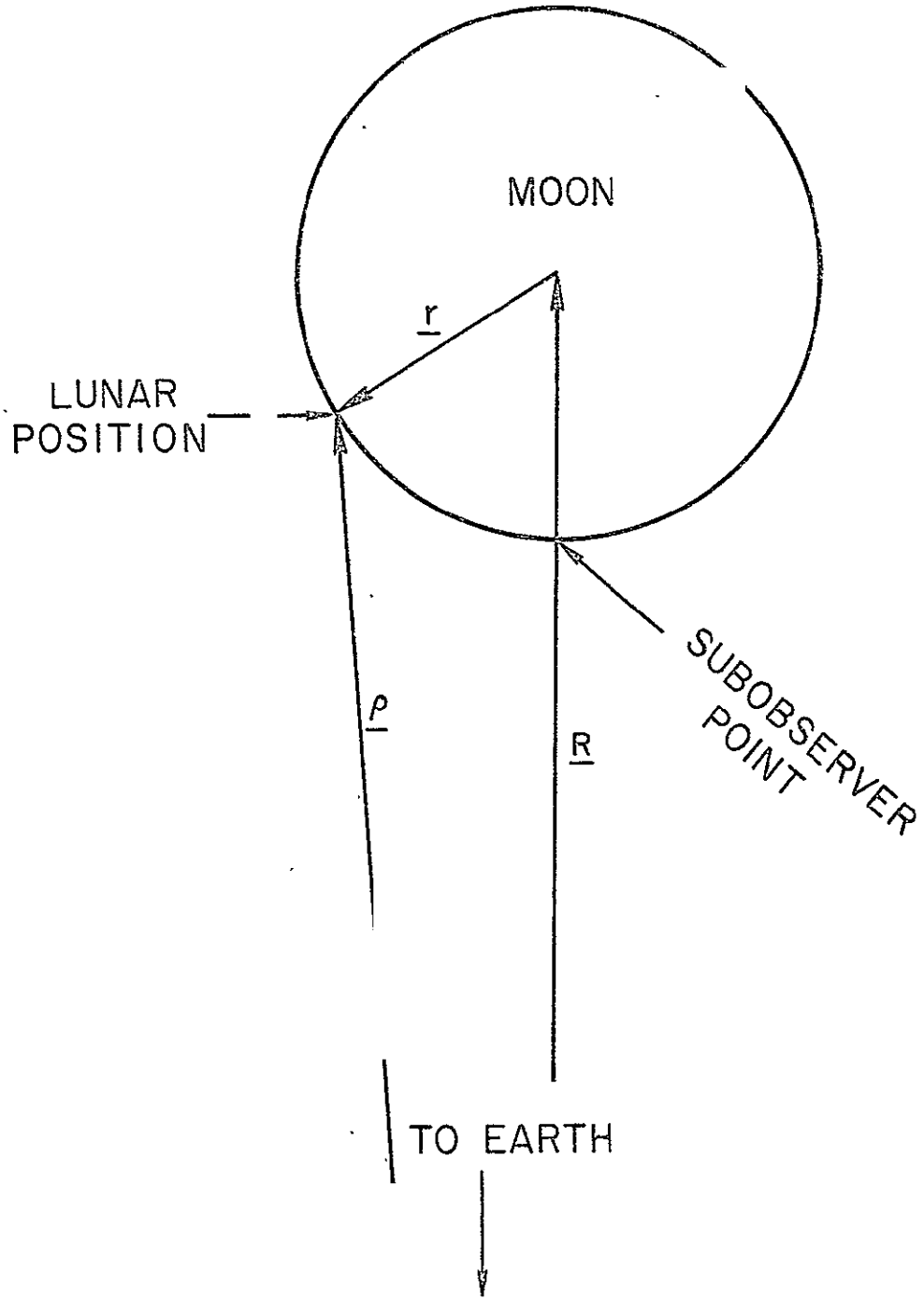

FIGURE 4. BASIC GEOMETRY FOR DERIVATION OF RELATIONSHIPS FOR LOCATING SENSOR POSITION ON THE LUNAR SURFACE.

$\underline{r}'$ = the vector from the center of the Moon to the lunar feature. It immediately follows from the above and Figure 3 that

$$\underline{r}' = \underline{\rho} - \underline{R} = (\rho\cos\alpha\cos\delta - R\cos\alpha_{\mathbb{D}}\cos\delta_{\mathbb{D}}\ ,\ \rho\sin\alpha\cos\delta - R\sin\alpha_{\mathbb{D}}\cos\delta_{\mathbb{D}}\ ,\ \rho\sin\delta - R\sin\delta_{\mathbb{D}}) \tag{8}$$

The vector $\underline{r}'$ is a selenocentric vector but lies in a coordinate system referenced to the Earth's rotational pole and the Vernal Equinox. However, it can be placed in the instantaneous observational coordinate system by two simple coordinate rotations. The first is a positive rotation through the angle $\alpha_{\mathbb{D}} - \frac{\pi}{2}$ about the z-axis to place the y-axis in the plane of the declination circle, pointing away from the Earth. The final rotation about the resultant x-axis through an angle of $\delta_{\mathbb{D}} + \frac{\pi}{2}$ places the z-axis along $\underline{R}$, pointing toward the Earth, and the y-axis pointing northward. Applying this transformation to $\underline{r}'$, we get

$$\underline{r} = \begin{bmatrix} 1 & 0 & 0 \\ 0 & -\sin\delta_{\mathbb{D}} & \cos\delta_{\mathbb{D}} \\ 0 & -\cos\delta_{\mathbb{D}} & -\sin\delta_{\mathbb{D}} \end{bmatrix} \begin{bmatrix} \sin\alpha_{\mathbb{D}} & -\cos\alpha_{\mathbb{D}} & 0 \\ \cos\alpha_{\mathbb{D}} & \sin\alpha_{\mathbb{D}} & 0 \\ 0 & 0 & 1 \end{bmatrix} \begin{bmatrix} \rho\cos\alpha\cos\delta - R\cos\alpha_{\mathbb{D}}\cos\delta_{\mathbb{D}} \\ \rho\sin\alpha\cos\delta - R\sin\alpha_{\mathbb{D}}\cos\delta_{\mathbb{D}} \\ \rho\sin\delta - R\sin\delta_{\mathbb{D}} \end{bmatrix}$$

$$= \begin{bmatrix} -\rho\cos\delta\sin(\alpha-\alpha_{\mathbb{D}}) \\ \rho(\sin\delta\cos\delta_{\mathbb{D}} - \sin\delta_{\mathbb{D}}\cos\delta\cos(\alpha-\alpha_{\mathbb{D}})) \\ R - \rho(\cos\delta\cos\delta_{\mathbb{D}}\cos(\alpha-\alpha_{\mathbb{D}}) + \sin\delta\sin\delta_{\mathbb{D}}) \end{bmatrix} \tag{9}$$

The vector $\underline{r}$ now can be directly related to the planar rectangular coordinates of the lunar disk by writing $\underline{r} \equiv r\,(x,y,z)$, where x, y, z are direction cosines. It immediately follows that

$$\begin{aligned} rx &= -\rho\cos\delta\sin(\alpha-\alpha_{\mathbb{D}}) \\ ry &= \rho(\sin\delta\cos\delta_{\mathbb{D}} - \sin\delta_{\mathbb{D}}\cos\delta\cos(\alpha-\alpha_{\mathbb{D}})) \\ rz &= R-\rho(\cos\delta\cos\delta_{\mathbb{D}}\cos(\alpha-\alpha_{\mathbb{D}}) + \sin\delta\sin\delta_{\mathbb{D}}) \end{aligned} \tag{10}$$

Equations (10) tie together the orientation of the telescope and the position of the sensor on the lunar surface. In the application of these relationships, it is useful to replace the right ascension (α) by the local hour angle (h) defined by

$$h = \theta - \alpha \tag{11}$$

where θ is the local sidereal time. Other useful definitions are the topocentric lunar semidiameter $s = \sin^{-1}(\frac{r}{R})$ and the difference coordinates $\tilde{h} = (h-h_{\mathcal{D}})/s$, $\tilde{\delta} = (\delta-\delta_{\mathcal{D}})/s$. The semidiameter is always less than 5 milliradians, and the difference coordinates range between -1 and 1 when the sensor is on the Moon. Small angle approximations then allow us to express (10) as follows:

$$s = \frac{r}{R};\quad 1 - sz = \frac{\rho}{R}$$

$$x = (1 - sz)\,\tilde{h}\cos\delta \tag{12}$$

$$y = (1 - sz)\,\tilde{\delta}$$

It having been established that the scanning motion of the telescope can be associated with a Cartesian coordinate system on the lunar disk, the transformation between this observational system and the selenographic system must be derived. The selenographic latitude and longitude of the subobserver point on the Moon is given by the topocentric librations in these same coordinates. A third angular relationship in the transformation is the topocentric position angle of the axis, defined as the angle between the observational y-axis and the projection of the Moon's rotational axis into the x-y plane. This angle is measured counterclockwise from the y-axis.

The transformation from the observational (x, y, z) to the selenographic (ζ, ξ, η) is accomplished by three rotations, as follows:

i) A positive rotation about the z-axis through the angle C, the position angle of the axis. This aligns the resultant y-axis with the projection of the rotational axis.

ii) A negative rotation about the resultant x-axis through the angle $\frac{\pi}{2} - b$, where b is the topocentric libration in latitude. This aligns the resultant z-axis with the Moon's rotational axis, the η-axis.

iii) A negative rotation about the η-axis through the angle $\frac{\pi}{2} + \ell$, where ℓ is the topocentric libration in longitude. The final orientation coincides with the selenographic axes.

The inverse transformation, (ζ, ξ, η) $\rightarrow$ (x, y, z), reverses the order and sign of the three rotations. The transformation matrix is

$$\begin{bmatrix} \zeta \\ \xi \\ \eta \end{bmatrix} = \begin{bmatrix} \cos(\frac{\pi}{2}+\ell) & -\sin(\frac{\pi}{2}+\ell) & 0 \\ \sin(\frac{\pi}{2}+\ell) & \cos(\frac{\pi}{2}+\ell) & 0 \\ 0 & 0 & 1 \end{bmatrix} \begin{bmatrix} 1 & 0 & 0 \\ 0 & \cos(\frac{\pi}{2}-b) & -\sin(\frac{\pi}{2}-b) \\ 0 & \sin(\frac{\pi}{2}-b) & \cos(\frac{\pi}{2}-b) \end{bmatrix} \begin{bmatrix} \cos C & \sin C & 0 \\ -\sin C & \cos C & 0 \\ 0 & 0 & 1 \end{bmatrix} \begin{bmatrix} x \\ y \\ z \end{bmatrix}$$

$$= \begin{bmatrix} \cos\ell \sin C \sin b - \sin\ell \cos C & -\sin\ell \sin C - \cos\ell \cos C \sin b & \cos\ell \cos b \\ \sin\ell \sin C \sin b + \cos\ell \cos C & \cos\ell \sin C - \sin\ell \cos C \sin b & \sin\ell \cos b \\ -\sin C \cos b & \cos C \cos b & \sin b \end{bmatrix} \begin{bmatrix} x \\ y \\ z \end{bmatrix} \quad (13)$$

Since the rotation is orthogonal, the inverse matrix is simply the transpose of the above. These matrices form the basis for fitting observed nighttime anomalies to known eclipse anomalies.

The topocentric librations used in (13) can be computed in two ways. The first method yields corrections to the geocentric librations tabulated in the Astronomical Ephemeris. The relationships are approximate and can be found in the back of the Astronomical Ephemeris in the "Explanation." This method requires second order interpolation of seven tabulated quantities from the ephemeris. The equations are straightforward and amenable to hand calculation.

When computing facilities are available, the work involved is reduced by solving the problem rigorously. The number of required interpolations is reduced to three. The computer program accepts the Moon's celestial coordinates at the time of observation, makes parallax corrections to these, and calculates the librations directly.

An error source occurs in the evolution of the transformation matrix during a set of observations, which can last for several hours. It is best to generate two or three matrices per set, depending on the total length of time involved. The error then can be directly evaluated.

b. Sensor Motion

The telescope points at (h,δ) in topocentric coordinates. If (h,δ) falls within the boundaries of the lunar disk, then the sensor location (x, y, z) on the Moon is given by

$$\begin{bmatrix} x \\ y \\ z \end{bmatrix} = \begin{bmatrix} \frac{l}{s} & \frac{\rho}{R} & \sin(\tilde{sh})\cos\delta \\ \frac{l}{s} & \frac{\rho}{R} & [\sin\delta\cos\delta_{\mathcal{D}} - \cos(\tilde{sh})\cos\delta\sin\delta_{\mathcal{D}}] \\ \frac{l}{s} & (1 - \frac{\rho}{R}[\sin\delta\sin\delta_{\mathcal{D}} + \cos(\tilde{sh})\cos\delta\cos\delta_{\mathcal{D}}]) \end{bmatrix} \qquad (14)$$

Equation (14) is simply a reformulation of (10).

The motion of the sensor (x, y, z) is a function of the combined motions of the telescope ($\dot{h}, \dot{\delta}$) and the Moon ($\dot{h}_\mathfrak{D}, \dot{\delta}_\mathfrak{D}$). The relationships are determined by taking the time derivative of each of the components of (14). The expressions become simpler if we work in terms of the conical coordinates defined as

$$x_c = \frac{x}{1-sz}$$
$$y_c = \frac{y}{1-sz} \qquad (15)$$

The leading terms in the time derivative of (15) are

$$\dot{x}_c = \dot{h}\cos\delta - \tilde{h}\cos\delta\left(s\tan\delta\frac{\dot{\delta}}{s} - s^2\tilde{\dot{\delta}}\dot{\delta}\right)$$
$$\dot{y}_c = \dot{\delta} + (\dot{h}\cos\delta)(\tilde{h}\cos\delta_\mathfrak{D})(s\tan\delta_\mathfrak{D}) \qquad (16)$$

For a right ascension scan, the leading term in $\dot{x}_c$ is four orders of magnitude larger than the second one. All the terms of $\dot{y}_c$ are small, and their importance is determined by estimating the displacement of a scan line over its length due to the presence of the small $\dot{y}_c$ component. Comparing this displacement to a resolution element, we find that the second term has marginal significance; and the leading term is important only if the telescope has no declination tracking motion ($\dot{\delta} = 0$). Motion for declination scans can also be determined from (16).

The topocentric motion of the Moon ($\dot{h}_\mathfrak{D}$, $\dot{\delta}_\mathfrak{D}$) can be obtained from the tabulated geocentric motions in right ascension and declination ($\dot{\alpha}_o$, $\dot{\delta}_o$), once the geocentric values have been corrected for apparent motion due to parallax and refraction. The corrections were formulated by Maxwell (1931) and are based on the relationships

$$h_\mathfrak{D} = h_o + \frac{\sin Z \sin Q}{\cos\delta_o}\left(\pi_\mathfrak{D} - \frac{K}{\cos Z}\right)$$
$$\delta_\mathfrak{D} = \delta_o - \sin Z\cos Q\left(\pi_\mathfrak{D} - \frac{K}{\cos Z}\right) \qquad (17)$$

where Z is the geocentric zenith angle, Q is the parallactic angle, $\pi_\mathfrak{D}$ is the Moon's horizontal parallax, and K is a constant describing atmospheric refraction. Shorthill and Saari (1961) accept Maxwell's value, K = 0.94 arc minutes; and I have done likewise.

Maxwell simply differentiated (17) with respect to time to obtain the corrections to the motion but neglected terms containing $\dot{\delta}_o$. I find this leads to an error in the topocentric motion of about 1%. The corrections I used are

$$\dot{h}_\mathfrak{D} = \dot{h}_o\left[1 + \frac{\pi_\mathfrak{D}\cos h_o\cos\phi}{\cos\delta_o} - K\left(\frac{\cos\phi}{\cos Z}\right)^2(1 + \tan\phi\tan\delta_o\cos h_o)\right]$$

$$\dot{\delta}_\mathfrak{D} = \dot{\delta}_o[1 + \pi_\mathfrak{D}\cos Z] - \dot{h}_o\sin h_o\cos\phi[\pi_\mathfrak{D}\sin\delta_o - K\sin\phi\sec^2 Z] \qquad (18)$$

where ϕ is the observer's latitude.

12. DATA PROCESSING

The data from the bolometer was digitized at the telescope and punched on paper tape in real time. The tapes were run through a tape-to-card reader, and the IBM cards, along with the observer's notes and printouts, were mailed to the Manned Spacecraft Center for analysis. At MSC the cards were compared with the original tapes to correct obvious formatting errors and then were processed on a Univac 1108 using a program written for that purpose in FORTRAN V. Several types of output were generated on the 1108:

a) The data points for each scan were printed in a compact but easily read form. On the same page was displayed certain information about the scan, which had been coded into the paper tape. The program had a limited ability to restore the least significant digit which was occasionally lost when the signal temporarily exceeded the dynamic range of the punch.

b) Each scan was graphically reproduced by a microfilm plotter.

c) With an input of the topocentric librations, the transformation matrix was calculated. The (ξ,η) coordinates were printed for a uniform grid in the (x, y) system.

d) Using the microfilm plotter, a circle with a superimposed rectangular grid was drawn, representing the (ξ,η) coordinate system. Equally spaced scan lines were plotted on this grid so that the scanned portion of the Moon could be determined approximately.

Hard copies of the plotted scans serve as the focus of the data reduction effort. Each trace is visually searched for thermal anomalies. The number of data points between each anomaly and the cold limb deflection is determined. For some of the scans the observer has noted the passage of the scan over a feature in the illuminated portion of the disk. The selenographic coordinates of the observed landmark are transformed into the conical observer coordinates on a Wang 700 programmable calculator. If the scanning speed of the telescope is known, the scan time to the cold limb and the limb coordinates can be calculated. This part of the program is also used to determine the number of data points between a known anomaly and the cold limb, should the anomaly appear on a scan. Once the limb coordinates have been computed, all anomalies on the scan can be located in selenographic coordinates simply by entering the number of data points separating them from the cold limb deflection.

In general, the above procedure does not result in unambiguous identifications of infrared anomalies. The more prominent anomalies are checked against a lunar map of eclipse isotherms constructed by Shorthill and Saari (1969, 1970). The scan locations often can be corrected in this manner. However, it has been found that the location errors can be large (up to two sensor diameters) and can be nonsystematic: Under these conditions, the identification of anomalies becomes a time-consuming iterative process. The abundance of thermal structure on the Moon and the difficulty of interpreting differential scans sometimes combine to thwart this strategy of identification. The confirmation of thermal structure differing from that of the eclipse becomes especially difficult.

TABLE I

LUNAR SCAN INFORMATION

	DATE	TYPE OF SCAN	PHASE	FRACTION ILLUMINATED	REMARKS
1	2/17/67	Dec.	Waxing	0.54	IBM card format garbled. No paper tapes available for correction. Observer notes incomplete.
2	3/07/67	Dec.	Waning	0.12	IBM cards garbled; no paper tape available. Scan locations poor.
3	3/14/67	Dec.	Waxing	0.12	Scans at very low gain. Little information.
4	3/15/67	Dec.	Waxing	0.19	First night of extensive coverage. Low gain. Large number of spikes due to malfunction of tape punch.
5	4/11/67	Dec.	Waxing	0.04	Good signal. Few notes due to small illuminated crescent. Some data spikes, but simultaneous strip chart available.
6	5/01/67	Dec.	Waning	0.48	Low gain. Lots of spikes. Trace noisy.
7	5/03/67	Dec.	Waning	0.29	Good signal, but trace was noisy.
8	5/13/67	Dec.	Waxing	0.18	Low gain; almost no signal.
9	5/14/67	Dec.	Waxing	0.27	Card format garbled. Data not plotted.
10	5/15/67	Dec.	Waxing	0.37	Good data.
11	6/01/67	Dec.	Waning	0.36	Good data.
12	6/06/67	Dec.	Waning	0.03	Nice data but difficult to analyze due to small crescent.
13	6/11/67	Dec.	Waxing	0.15	Lots of equipment trouble. No cards available.
14	12/06/67	Dec.	Waxing	0.33	Poor signal. Unusual large scale structure.
15	2/03/68	R.A.	Waxing	0.27	Good data. Scans alternate eastward and westward.
16	2/05/68	R.A.	Waxing	0.45	Good data. Scans to left only.
17	3/24/68	R.A.	Waning	0.18	Excellent signal.
18	4/01/68	R.A.	Waxing	0.14	Good data.
19	4/05/68	R.A.	Waxing	0.49	See scattered radiation from illuminated crescent.
20	4/29/68	R.A.	Waxing	0.05	Limb deflection good, but scans relatively featureless. Notes poor due to small crescent.
21	4/30/68	R.A.	Waxing	0.10	Small amount of data due to cloudiness.
22	5/19/68	R.A.	Waning	0.47	Quite noisy; limb deflection unidentifiable.
23	5/20/68	R.A.	Waning	0.36	Signal low but data useful.
24	5/21/68	R.A.	Waning	0.27	Good data.
25	5/22/68	R.A.	Waning	0.19	Poor signal. No limb deflection.
26	5/23/68	R.A.	Waning	0.12	Good data.
27	5/30/68	R.A.	Waxing	0.12	Lots of data but noisy. Limb sometines difficult to identify.
28	5/31/68	R.A.	Waxing	0.19	Same as 5/30.
29	6/01/68	R.A.	Waxing	0.28	Poor signal.

13. DISCUSSION OF THE MEASUREMENTS

Table I, entitled "Lunar Scan Information," contains a brief summary of lunar nighttime observations considered in this paper. We have taken data which gives excellent coverage from a 50% illuminated, waning Moon (third quarter) through new Moon to a 50% illuminated, waxing Moon (first quarter). If the Moon is more than 50% illuminated, scattered radiation from the bright portion becomes a problem in the darkside scans. Considering the variety of phases and libration angles it is estimated that most of the lunar hemisphere facing the Earth has been scanned at one time or another.

To date, this vast array of information has resisted systematic correlation for three reasons. First, we have been unsuccessful in integrating the scans. There exist instabilities in the data which prevent reconstruction of the integral trace in a way allowing scan-to-scan correlation within an observation set. Thus it is impossible to assign a radiance value to a point on the scan. This even includes values relative to the limb deflection. Some hope for recovery of radiance values may lie with Fourier transform techniques. This avenue has not been completely explored.

Correlations between observation sets have been thwarted by a lack of standardization in the data. Very seldom were any standard astronomical infrared sources monitored during a set of observations. In the future, lunar features themselves can be used as standards; but the necessary groundwork for this has not been performed.

Finally, the quality of the data varies significantly among the sets. It requires an enormous amount of time to read paper tapes by hand for correction of garbled sets of IBM cards, to rid traces of spikes due to malfunctions of the data punch, or to reconstruct a scan raster by making guesses at the identity of features. For these reasons, the best data has been analyzed first; and this report is based primarily on right ascension scans with good signals.

The discussion has been broken down into the identification of prominent anomalies, computed temperatures of certain cold limb deflections, and analysis of large scale regions of anomalous cooling on the waning Moon.

a. Thermal Anomalies

In previous discussions it has been shown that understanding the thermal parameters of a lunar surface feature depends on monitoring its temperature as a function of time. Unfortunately, the deflection on a differential scan is not proportional to an object's temperature but rather the temperature contrast between it and its environs. Knowledge of the variation in this contrast is potentially useful, but comparisons between observation sets is currently not possible for reasons discussed at the beginning of this section. In addition, a scanning technique has the inherent disadvantage that features can fall just to one side of a scan path and be recorded on the scan at reduced intensity.

A current list of identified anomalies is given in the Appendix. For each anomaly is given its coordinates in selenographic longitude

and latitude. The number of days since sunset at that location is listed in the third column. Multiple entries for a feature implies that it was found on more than one set of observations. The lunar night is 14.8 days in duration.

The two most conspicuous thermal features on the near side of the Moon are the craters Tycho and Copernicus. Tycho is far brighter than any other nighttime object and has never failed to peg the recorder when it was scanned. The extraordinarily large signal is probably explainable in terms of the spatial extent of the rock fields associated with the feature rather than any peculiar thermal properties. The Copernican anomaly is no brighter than some other features but is distinctive in its characteristically broad shape. It appears even when the signal to noise ratio is low, and the scans are relatively featureless. There is some evidence that the anomaly is more extensive in the East-West direction than the North-South. Figure 3 compares the Tycho and Copernicus deflections on the same day of observation.

A third distinctive thermal signature on the nighttime Moon is that of Mare Humorum. On a set of scans running northeast-southwest, it displays consistently a "stairstep anomaly" structure (Figure 5) from the vicinity of Gassendi southward to Vitello. After the second "stair step" there is generally evidence of a continuing fall in temperature, but the meaning of this part of the feature is very difficult to interpret without an integrated scan. The first peak defines the western border of the enhancement. A plot of the position of this peak for ten scans shows that it falls on the western rim of Mare Humorum to an accuracy well within the location of the scan. The position of the corresponding

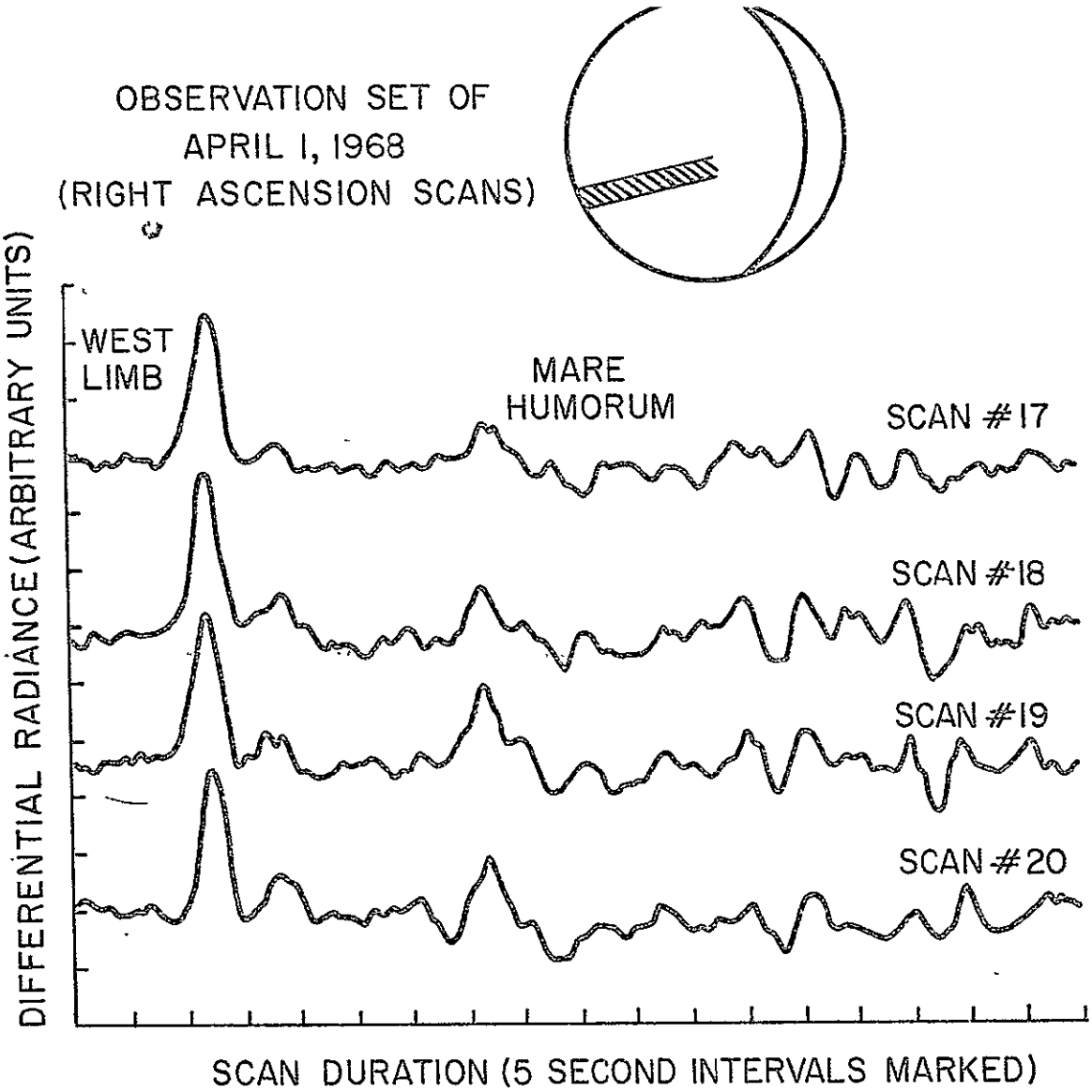

FIGURE 5. A SET OF 11 SCANS STEPPING THROUGH MARE HUMORUM. SCAN LINES TRAVEL IN A NORTHEAST-SOUTHWEST DIRECTION; DISPLACEMENT OF THE SCANS IS IN A DIRECTION PERPENDICULAR TO THIS. THE HATCHED AREA ON THE LUNAR DISK AT THE TOP OF THE FIGURE CORRESPONDS TO THE COVERAGE OF THE SCANS IN THIS FIGURE.

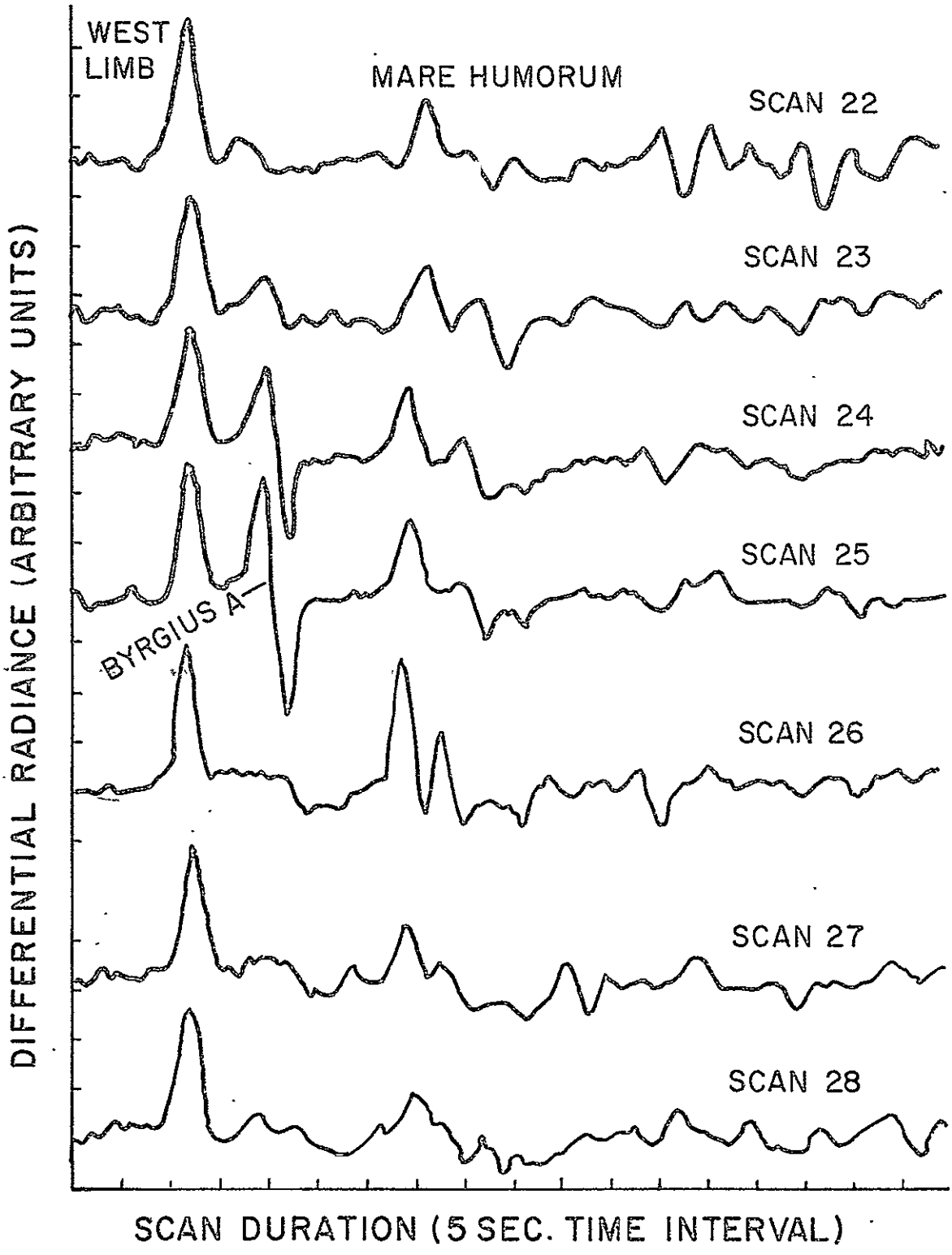

FIGURE 5 (CONTINUED)

negative peak in general falls somewhat within the eastern boundary of the mare. However, the structure on the trace is complicated, and it is difficult to say that the first negative dip always represents the eastern end of the anomaly. The mare, as a whole, appears uniformly enhanced, with the exception of a few isolated hot spots.

In general, the nighttime Moon exhibits as much or more thermal structure than the eclipsed Moon. There exists some evidence for eclipse anomalies which are not nighttime anomalies. It is difficult to confirm such a phenomenon, especially on a limited data set, since the recorded signal from a point source is critically dependent on the exact sensor path. On the other hand it is important to be alert for such a feature. A structure which remains warmer than its surroundings for a few hours (or a few days) and then comes into equilibrium clearly exhibits a total heat content which falls within definite limits. A model for such a feature might be a surface distribution of thermally isolated rocks, typically a few tens of centimeters in size.

Cold anomalies are of interest but are very difficult to verify due to the difficulties of interpreting differential scans. Such features are certainly not very prominent. A current candidate is the crater Agatharcides. It was the location calculated for a small "inverse anomaly" on a scan line. A check showed that it is a locally thermally depressed region. Its position on the scans for a second set of observations was calculated, and the data was examined. At the appropriate location was a poorly formed, but possible, inverse anomaly. Unfortunately the discovery is not particularly startling since Agatharcides lies on

a tongue of highland material between Mare Humorum and Mare Nubium, two thermally active maria.

In addition to Mare Humorum, another extended thermal feature exists on the nighttime Moon. The feature is associated with the Marius Hills region, and extends from Aristarchus and Herodotus southward to just beyond Marius. At approximately 8° North latitude the anomaly has disappeared. Complicating the thermal structure due to the ridge system is the presence of the deflections due to Marius and its alphabetical namesakes A, B, and C. Other enhanced ridges exist such as the one running northwest-southeast through the crater Herigonius.

b. Cold Limb Temperatures

Following the set of observations for April 5, 1968, 11 deflections were made on the planet Jupiter. The planet had a zenith angle of 45°.1 (1.4 air masses), and the signal to noise ratio of the deflections ran in the range 20-40. A typical reading on the sky or the planet consisted of 10-40 data points, although some were more. An average of each set was taken as the reading, and contiguous sky-planet readings were subtracted to give the deflection. The noise associated a given deflection was determined by summing the standard deviations of the two readings involved. The 11 deflections were averaged to arrive at a value for the planetary signal. The standard deviation associated with the final average was ± 4%.

TABLE II

Limb Brightness Temperatures for April 5, 1968 Observations
(Jovian Brightness Temperature at 22 microns = 128°K)

Scan No.	Temperature (°K)	Sensor Location
3	95.6	81W 28N
4	97.2	82W 26N
5	97.3	82W 25N
7	98.1	82W 23N
8	96.5	82W 22N
9	99.3	83W 21N
10	94.9	83W 20N
14	99.6	83W 19N
15	99.1	83W 18N
16	94.9	84W 16N
17	98.5	84W 15N
18	95.2	84W 15N
19	95.4	84W 14N
20	97.9	84W 13N
21	95.7	84W 12N
25	98.3	85W 10N
27	95.7	85W 9N
28	96.9	85W 9N

(Note: The libration in longitude at the times of observation was approximately 6W. This places the cold limb at approximately 96W. Identical sensor locations for different scans means that the corrected scan position places the sensor location within $\pm$ 0.5° of the given location. The estimated error in temperature is $\pm$ 6.0°K)

This measurement of Jupiter was used as a calibration to determine the temperatures associated with the cold limb deflections on those scans located by the observer, assuming a planetary temperature of $128 \pm 10^{o}K$ (Armstrong, 1971). The resultant temperatures and the sensor locations are given in Table II for 22 deflections. To obtain the values the lunar deflections were compared to the Jovian deflection after corrections for differing amplifier gains and differing air masses. The ratio of the corrected deflections is equal to the ratio of the emitted fluxes from the two objects. No correction for beam size was necessary since both sources filled the beam. The conversions between relative flux and temperature were made with a flux-temperature plot which takes into account the spectral properties of the filter and atmosphere combined.

An uncertainty of approximately a degree in each coordinate of the sensor location arises from computational approximations. The random uncertainty due to observer error in locating the scan should be on the order of half a degree in each coordinate. A larger systematic error could arise from offsets in the alignment of the main telescope and the guide telescope.

The existence of "hot spots" on the Jovian disk at 22 microns complicates the question of the uncertainty in the Jovian flux since the sensor resolution was less than the planetary disk. I feel that the large number of deflections which are relatively consistant among themselves allows the use of the effective temperature for the spatially integrated disk. A flux uncertainty of 40% of this value affects the

computed lunar temperature by 5.8°K at 97°K. The uncertainties in the atmospheric extinction coefficient and the planetary deflection are 1.5°K and 0.7°K, respectively. Error due to inaccuracy of the effective wavelength of the system's spectral response is only 0.1°K. The total error from these sources is calculated to be $\pm$ 6.0°K for a computed limb temperature of 97°K.

c. Large Scale Features on the Scan

The lunar nighttime cooling curve can be divided into two parts. Immediately after sunset, the cooling is relatively rapid; and the subsurface gradients are nonlinear. The temperature profile as a function of time (or, equivalently, as a function of longitude) is also nonlinear. When the surface temperature falls to approximately 100°K, the radiative heat leak at the surface becomes small; and the thermal gradients beneath the surface reach a steady state. The temperature profile becomes more nearly linear and, in fact, almost constant.

These two thermal regimes show up quite differently on a differential infrared scan. The later regime gives a very flat trace. This is seen clearly on scans of the waxing Moon where the baseline is quite flat between the cold limb deflection on one end and the saturation due to the sunrise terminator on the other. The nonlinear regime, on the other hand, gives a nonlinear trace. The sensitivity of the differential technique is such that this gradient in the trace can quickly exceed the dynamic range of the system.

Since the nonlinear regime falls close to the sunset terminator, it is important to be able to distinguish an actual rise in nighttime temperature from an increasing signal due to scattered radiation in the telescope from the nearby bright crescent. The 22-micron flux from an illuminated lunar area is one or two orders of magnitude greater than that from a nighttime area. Scattered radiation from the bright crescent can be evaluated by examining scans of the waxing Moon. The dark side scan should be flat right up to the terminator. This was found to be the case on all but one set of observations. The anomalous set was distinctive in two respects. The Moon was more full than on any other similar set, and the gain on the amplifiers was at least 1.6 times higher than any other set. While scattered radiation can occur, it is only a problem when the Moon is between first quarter and third quarter.

Six sets of right ascension scans on the waning Moon have been examined for evidence of the existence of the two types of cooling regimes. Of these sets, five were taken on consecutive days from May 19 through May 23, 1968. The sixth set is that of March 24, 1968. On May 19, the Moon is 47% illuminated, the terminator being located at approximately 3.5^{o} West longitude. The signal to noise ratio is very poor, and cold limb deflections cannot be identified. All scans show a steep gradient in the signal, climbing until the data system saturated. The obvious conclusion is that most of the dark Moon is in the first, nonlinear cooling regime.

The cold limb deflections for the May 22 set are also absent, but luckily on March 24 the Moon was at the exact same phase as on May 22.

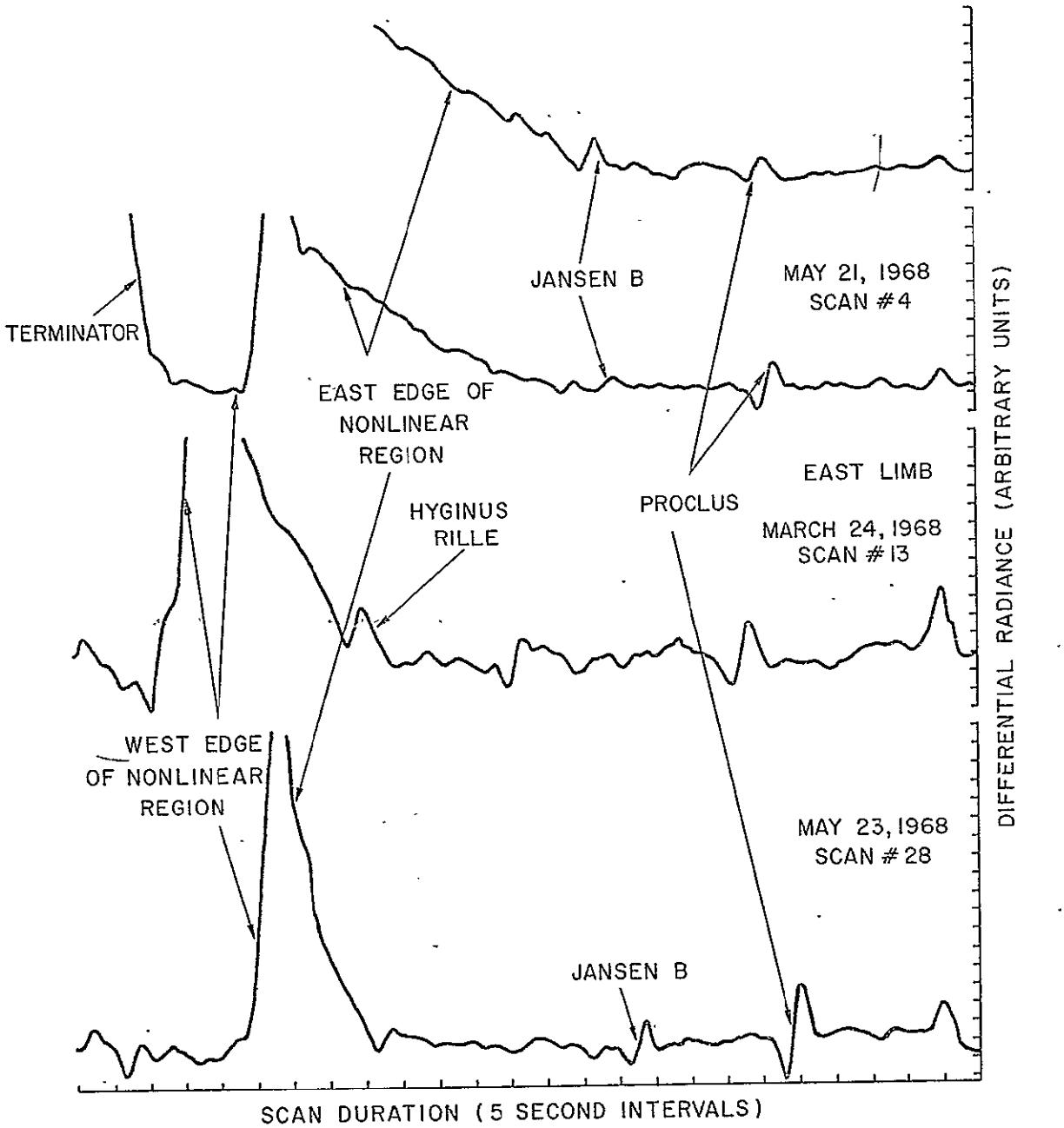

FIGURE 6. SCANS THROUGH THE CRATER PROCLUS FOR 4 SUCCESSIVE PHASES OF THE WANING MOON, ILLUSTRATING THE CHANGING STRUCTURE OF THE NONLINEAR COOLING REGION WITH TIME. POINT-BY-POINT COMPARISONS CANNOT BE MADE IN THIS FIGURE DUE TO DIFFERENT LIBRATIONS LUNAR DISK SIZE.

Four traces from the sets of May 20, May 21, March 24, and May 23 are depicted on Figure 6. All scans on the figure contain the thermal anomaly due to the crater Proclus. In each case it is the first major anomaly after the cold limb deflection (proceeding from left to right). The actual paths of the scans differ slightly due to different librations. The abscissa of the plots is time, and therefore the scale on the Moon differs slightly due to different sizes of the apparent disk at the time of observation.

A study of these traces reveals an interesting phenomenon. The flat portion of the scan between the cold limb and the onset of the gradient becomes longer on each day. This would be expected since the transition between the two cooling regimes would follow the sunset terminator westward. However, beginning on the May 21 set of observations, the trace does not continue to climb to saturation but rather falls abruptly so that another flat portion occurs on the scan before the terminator is encountered. The resulting structure is a large hump in the middle of the scan.

The eastern edge of the hump (representing the transition between the two regimes) falls nicely along lines of constant longitude, as determined from a series of scans in the same set of observations. There is some scatter in longitude amounting to two or three degrees on either side of an average, but this could be a result of errors in locating the edge of the hump. From the data in Figure 7 and Appendix B, it can be seen that the transition occurs approximately 4 days after sunset (45° of longitude east of the sunset terminator).

The western edge of the nonlinear region neatly traces out the boundary between the central highlands and the western maria. The

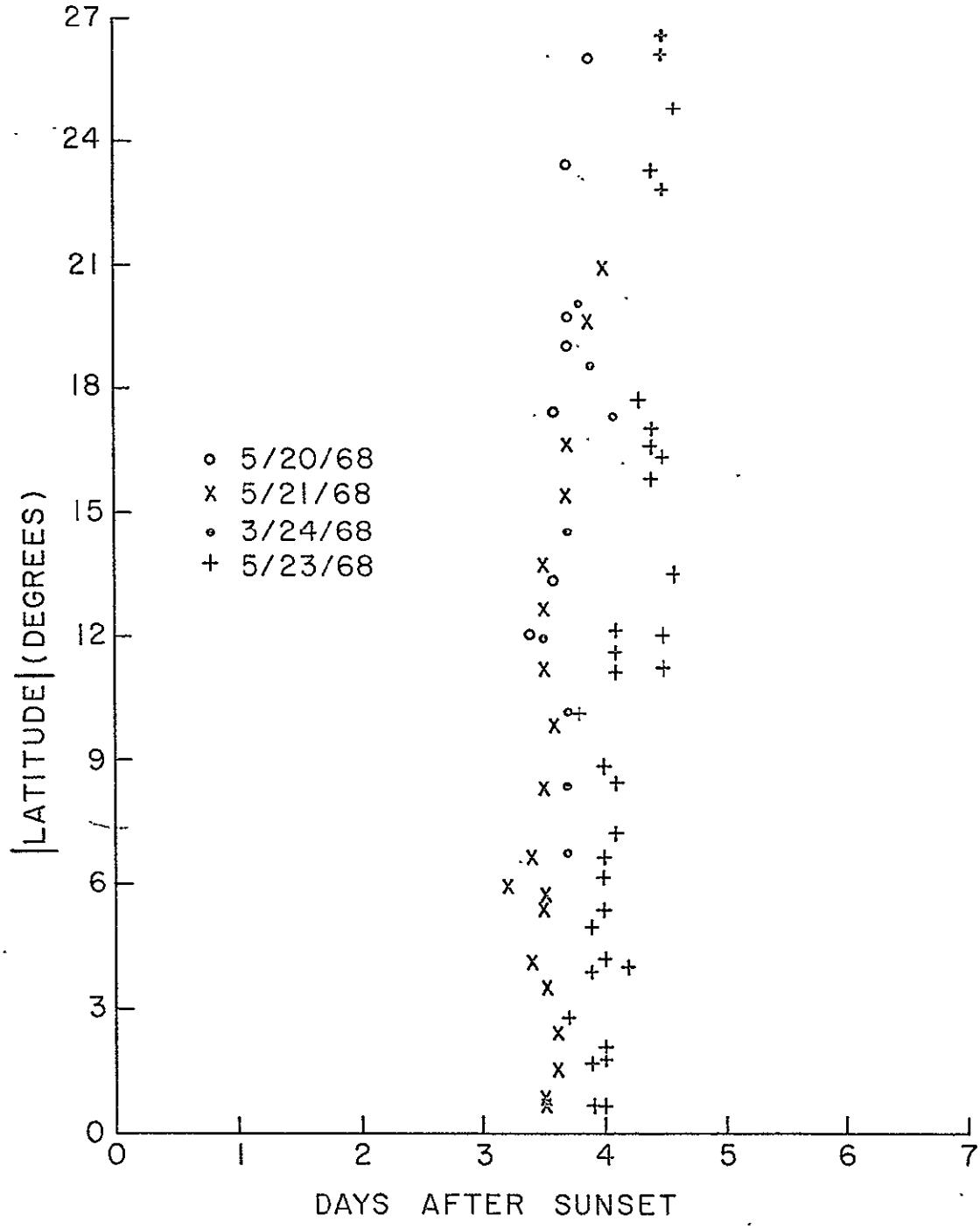

FIGURE 7. DATA TABULATED IN APPENDIX B. MANY LOCATIONS WERE DETERMINED FOR THE EASTERN EDGE OF THE NONLINEAR COOLING REGION. THE ABSOLUTE VALUE OF THEIR LATITUDES ARE PLOTTED AGAINST THEIR POSITION RELATIVE TO THE SUNSET TERMINATOR.

line runs along the western and southern boundaries of the Copernican highlands and along the northern and eastern boundaries of Mare Nubium. As the scans move south of Mare Nubium, and thus fall along highlands for their entire length, the humps become broad and indistinct. The scans do not go far enough northward to include the Imbrium-Apennine boundary. This boundary is the same for the sets of May 21, March 24, and May 23. These three sets are the equivalent of three consecutive days of observation. On the May 20, the observation set prior to the appearance of the humps, the terminator lies along the eastern edge of Mare Nubium.

It is difficult to make quantitative statements about the thermal properties of the Moon from these scans, but a few observations are pertinent. The edges of the humps are quite distinct on the scans. Unless a thermal feature sits right on the boundary, it is easy to pick out the point (to within a resolution element) where the scan baseline ceases to be flat. In other words, the transition in the Moon's thermal profile are quite distinct. The definitive nature of the transition and its consistency of behavior strongly imply that we are seeing a fundamental difference in the cooling curves of the maria and the highlands.

The data plotted on Figure 7 shows that the transition accurs systematically later in the May 23 set than at the preceding phases. A study of the locations in Appendix B reveals that positions for the earlier phases tend to follow the boundaries between the highlands and the eastern maria. Thus it appears that the true time lag associated with the transition may be the 4 to 4.5 days given in the last data set.

A proper explanation of the phenomenon depends strongly on the shape and value of the actual flux distribution. Attempts to integrate the scans and reconstruct the distribution yielded an unacceptable variety of shapes. However, the representation in Figure 8a and 8b gives the basic ingredients to the situation.

Figure 8(a) is a simplified differential scan with a "hump" in it. The hump is approximately triangular in shape. Figure 8(b) is the reconstructed scan. The gradients in (b) (and therefore the levels) are uncertain because the levels in (a) are uncertain. One interesting point is that the transitions marked 1 and 2 may not be obvious in the reconstructed scan although they are dramatic in the differential scan.

Figure 9 is a published scan by Murray and Wildey (1964) which covers the anomalous region during the correct phase of the Moon. It is the only darkside scan of the region which could be found in the literature. Note that the authors refer to the thermal plateau on the scan as a Type B anomaly. This notation means that a thermal rise out of a colder region never reversed itself to become a point anomaly. On the reverse scan over the same area the plateau is not so prominent. This is apparently due to increased sky noise during the transition from the colder region to the warmer region. From the information in this report, we can confidently assign the location of the plateau to the portion of Mare Nubium between Gassendi and Arzachel.

An explanation for the nonlinear cooling behavior of the highlands may lie in the physiography of the region. The highlands are much rougher on a large scale than the maria, and this roughness affects

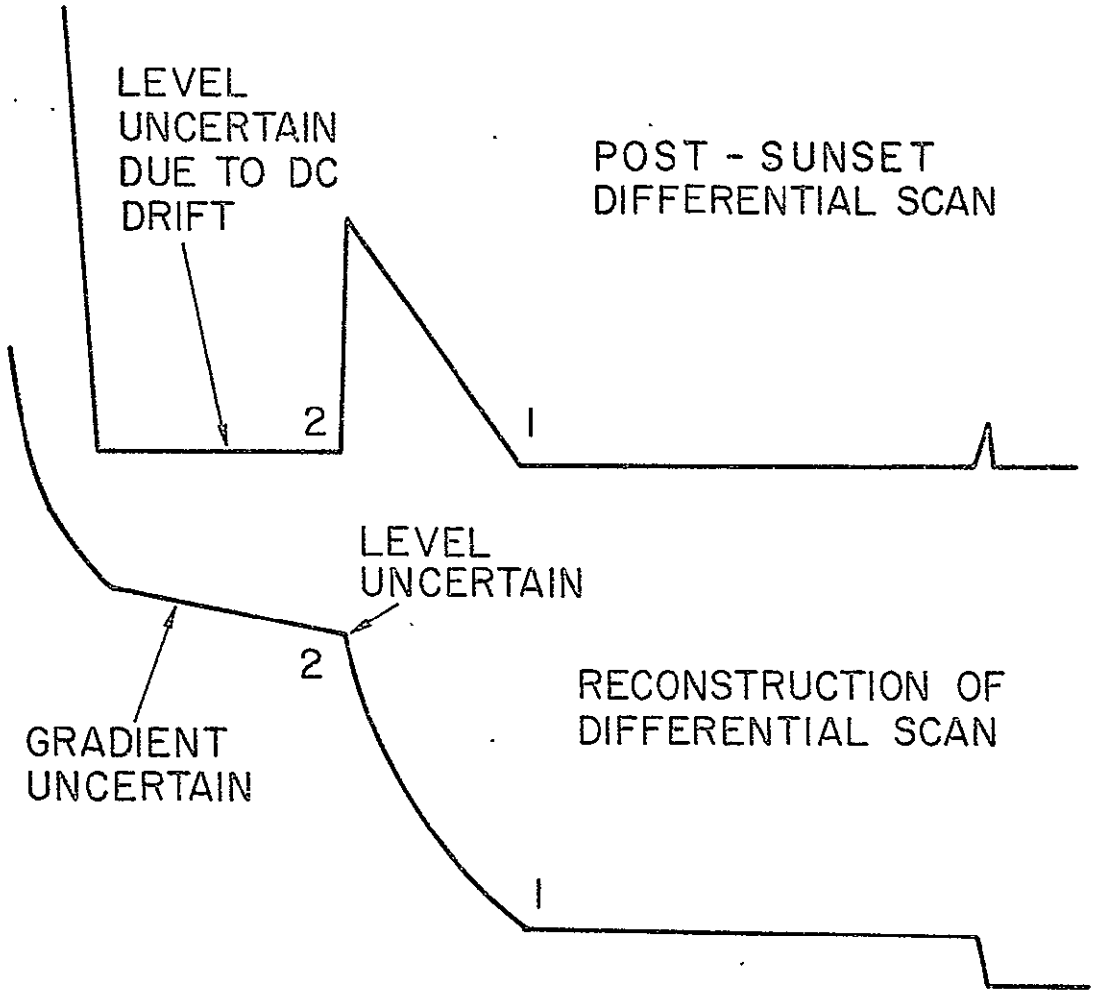

FIGURE 8. SIMPLIFIED VERSION OF A POST-SUNSET DIFFERENTIAL SCAN ILLUSTRATING THE NATURE OF THE RECONSTRUCTED SCAN AND THE ASSOCIATED UNCERTAINTIES.

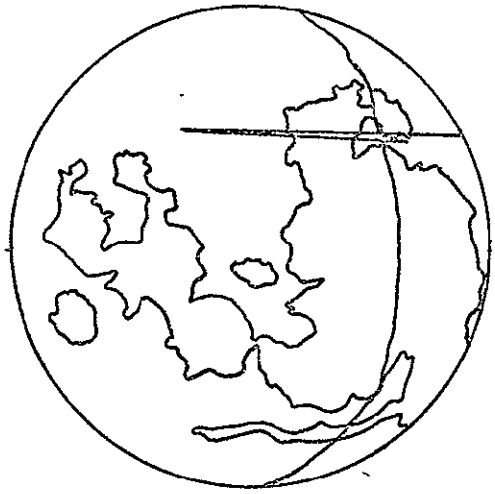

AUG 24-25 1962

25.0 DAYS

13^h U.T.

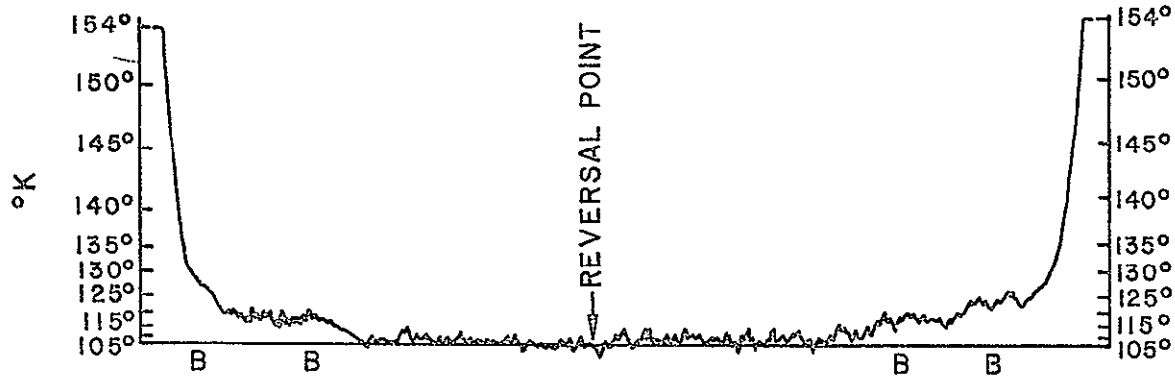

FIGURE 9. POST-SUNSET DARKSIDE SCAN ACROSS MARE NUBIUM FROM MURRAY AND WILDEY (1964).

the temperature distribution in the region. A study of isothermal maps of lunar regions prior to local sunset (Saari and Shorthill, 1967) demonstrates the difference. The isotherms in the maria tend to follow lines of longitude and are regularly spaced. The contours in the highlands are quite irregular, and one easily sees crater shapes in them.

The crater rims tilted toward the west receive fairly direct solar illumination until the Sun disappears beneath the horizon. Early in the lunar night the west faces of elevated surfaces (rims and mountains) will be much warmer than the surrounding topography or than a mare at a comparable time of (lunar) day.

The detector at the telescope measures the total thermal flux from within a resolution element. (At the subearth point, a resolution element is a circle roughly 50 kilometers in diameter.) Since the flux within the spectral bandpass of the sensor is approximately an exponential function of temperature, the hotter regions influence the total flux from an element far out of proportion to their actual surface area. After sunset, the warmer surfaces cool rapidly because the radiative energy loss is proportional to the fourth power of the surface temperature.

Initially the flux from the resolution element will decrease rapidly after sunset as the hot areas cool. With their falling temperature, their relative influence within the resolution element also decreases. The combination of the two effects causes the rate of decrease of flux to also diminish with time. This fact is then consistent with the gradient on the differential scan.

This qualitative explanation involving roughness is attractive because it utilizes a well known difference between the maria and the highlands. However, it apparently doesn't explain the well defined break in the differential curve at the eastern edge of the nonlinear region. The flux distribution should be quite smooth, and the transition should be very vague. Finally, such an effect should not last for 4 days. The lunar surface has a small thermal inertia and reacts quickly to changes in solar heating. The point obviously needs further analysis.

An alternative explanation invokes a significant rock population in the highlands. Roelof (1968) demonstrated by analysis that submeter rocks remain warmer than the soil background after sunset due to continued direct solar illumination at low sun angles. Depending on the size of the rock, it remains warmer only for part of the night and then becomes slightly cooler than the soil. Thus a rock population represents a hot component which is still cooling at the time it disappears into the soil background. The differential trace would show the necessary break in slope. To remain warm for 4 days, the rocks would have to be tens of centimeters in size.

The problem with this model lies in the geological explanation of the existence of a significant rock population in the ancient highlands despite the known erosional, soil-forming processes on the Moon. However, it is also known that impact processes can cause lithification. Interestingly enough, such a rock distribution would neatly explain the radar enhancement of the highlands over the maria (S. H. Zisk, private communication).

14. FURTHER WORK

The nighttime Moon has been scanned at a variety of phases, but the data collected falls short of being quantitative and definitive. The lunar midnight temperature has been measured with the differential scanning technique in work published elsewhere (Mendell and Low, 1970).

The need for thermal maps of the dark Moon is now greater than ever. In addition to leading to an understanding of thermal anomalies, such maps would also define the cooling properties of the highlands, the importance of which has been outlined in this report.

The problems associated with nighttime mapping should yield to adequate preparation and refined observational technique. It can be seen from the presented measurements that signal to noise is no problem with the Low bolometer under reasonable atmospheric conditions. The sensitivity of the system may be sufficient to allow a much wider sensor spacing, comparable to a lunar radius. The processing electronics must be carefully designed to eliminate droop.

In the present work, the telescope was used to simultaneously track the Moon and scan across it. If the tracking and guiding functions can be segregated, then the scan raster can be made more stable and the scans can be located more accurately. One promising technique consists of doing the scanning by driving the secondary mirror while the telescope drive is used only for tracking the Moon. A reliable and complete data acquisition system is the final link in a successful mapping operation.

Planning is under way for further mapping of the Moon. It is anticipated that successful completion of this task will give insight to lunar surface processes and history.

15. APPENDIX A

Locations Associated with Nighttime Thermal Anomalies

	Feature	Location		Days After Sunset
1.	Abulfeda A	10.8E	16.4S	12.0
2.	Abulfeda E	10.2E	16.7S	11.9
3.	Abulfeda Q	12.3E	12.8S	12.1
4.	Agatharcides A	28.4W	23.3S	8.8
5.	Archimedes	4.0W	29.7N	10.8
6.	Aristarchus	47.6W	23.7N	7.2
				11.3
7.	Aristillus	1.2E	33.8N	11.2
8.	Beaumont D	26.2E	17.1S	13.2
9.	Bessarion D	41.7W	19.8N	11.7
10.	Bessel	17.9E	21.7N	4.3
				5.3
11.	Birt	8.5W	22.3S	10.4
12.	Bode A	1.2W	9.0N	2.7
				14.2
13.	Bode G	3.5W	6.3N	14.0
14.	Bonpland E	22.6W	9.8S	12.5
15.	Bonpland H	19.9W	11.4S	2.2
				9.4
				12.7
16.	Boscovich	11.1E	9.8N	4.7
17.	Brayley C	39.4W	21.3N	11.9

	Feature	Location		Days After Sunset
18.	Bruce	0.4E	1.1N	1.8
19.	Bullialdus	22.2W	20.7S	9.3
20.	Byrgius A	63.8W	24.6S	5.8
				9.1
21.	Campanus	27.7W	28.0S	8.8
22.	Campanus B	29.2W	29.3S	8.7
23.	Carlini D	16.0W	33.0N	9.8
24.	Cassini K	4.0E	45.0N	11.5
25.	Cauchy	38.6E	9.6N	4.9
				7.0
26.	Cavalerius	66.9W	5.1N	9.7
27.	Censorinus	32.7E	0.4S	4.5
				6.5
				13.8
28.	Copernicus	20.0W	9.7N	1.2
				2.2
				7.8
				9.5
				10.6
				12.7
				13.5
29.	Copernicus C	15.4W	7.1N	1.6
30.	Copernicus H	18.3W	6.9N	1.3
				12.8
				13.7

	Feature	Location		Days After Sunset
31.	Darney C	26.0W	14.1S	8.9
32.	Dawes	26.3E	17.2N	2.9
				5.0
				6.0
33.	Dionysius	17.2E	2.8N	3.2
				5.2
34.	Diophantus	34.3W	27.6N	8.3
35.	Doppelmayer L	40.5W	23.6S	7.8
36.	Draper C	21.5W	17.0N	9.4
				10.5
				13.4
37.	Eimmart D	69.0E	23.0N	6.4
				8.5
				9.5
38.	Encke C	36.4W	0.6N	12.2
39.	Encke X	40.2W	0.9N	7.8
				11.0
				11.9
40.	Euclides	29.5W	7.4S	1.4
41.	Euclides B	30.3W	11.8S	1.4
42.	Euclides C	30.0W	13.3S	1.4
				8.6
				1.9
43.	Flamsteed	44.3W	4.5S	10.7

	Feature	Location		Days After Sunset
44.	Flamsteed A	42.9W	7.9S	7.6
45.	Flamsteed B	43.7W	5.9S	10.7
46.	Flamsteed GC	52.1W	3.5S	10.1
47.	Fourier C	52.0W	28.6S	6.8
48.	Galilaei	62.7W	10.5N	10.0
49.	Galilaei A	62.9W	11.7N	10.0
50.	Gambart A	18.7W	1.0N	1.3
				12.8
				13.6
51.	Gambart B	11.5W	2.2N	1.9
				13.4
				14.2
52.	Gambart C	11.8W	3.3N	1.9
				13.4
				14.2
53.	Gassendi A	39.7W	15.5S	7.8
54.	Gassendi G	44.6W	16.7S	7.5
55.	Gassendi J	37.0W	21.6S	8.0
56.	Godin	10.2E	1.8N	2.6
				4.7
57.	Guericke C	11.5W	11.5S	2.9
				10.1
				13.4

	Feature	Location		Days After Sunset
58.	Guericke D	14.6W	11.9S	2.6
59.	Guericke E	12.0W	10.0S	13.3
60.	Heinsius A	17.5W	39.6S	9.7
61.	Hell QA	4.4W	33.0S	1.4
				10.8
62.	Herigonius	33.9W	13.4S	8.3
				11.5
63.	Hesiodus B	17.5W	27.1S	9.6
64.	Hesiodus E	15.3W	27.8S	9.8
65.	Hooke D	55.7E	40.6N	8.4
66.	Hortensius	28.0W	6.5N	12.9
67.	Hortensius A	30.7W	4.4N	1.3
68.	Hortensius C	26.7W	5.9N	1.6
				12.1
				13.0
69.	Hyginus Rille	7E	7N	1
				3
				4
				12
70.	Jansen B	26.6E	10.6N	2.9
				4.0
				6.0
71.	Jansen E	27.8E	14.4N	6.1
72.	Jansen F	31.0E	12.5N	4.3

	Feature	Location		Days After Sunset
73.	Kepler	38.0W	8.1N	0.7
				8.0
				9.2
				12.0
74.	Kies A	22.7W	28.3S	9.2
75.	Kies C	26.1W	26.0S	8.9
76.	Kies D	18.4W	24.9S	9.6
77.	Lagrange C	65.0W	29.9S	5.8
78.	Lalande	8.6W	4.5S	14.5
79.	Langrenus	60.9E	8.9S	6.8
80.	Lansberg A	31.1W	0.2N	1.3
				8.6
81.	Lansberg D	30.6W	3.0S	1.3
				11.8
82.	Lassell D	10.5W	14.5S	0.9
				10.2
				13.5
83.	Letronne D	37.8W	9.4S	11.2
84.	Linne	11.7E	27.7N	4.8
85.	Lippershey T	11.1W	25.2S	10.2
86.	Lubiniezky G	20.2W	15.3S	9.4
				12.7
87.	Lubiniezky H	21.1W	17.0S	9.4
				12.6

	Feature	Location		Days After Sunset
88.	Macrobius A	40.3E	19.5N	6.1
				7.1
89.	Macrobius B	40.8E	20.9N	6.2
				7.2
90.	Madler	29.7E	11.0S	13.5
91.	Manilius C	10.3E	12.0S	3.7
92.	Manners	20.0E	4.5N	5.5
93.	Marius A	46.0W	12.6N	7.3
				11.4
94.	Marius C	47.5W	13.9N	7.2
				11.3
95.	Marius D	45.0W	11.4N	7.4
96.	Marius L	55.6W	15.8N	10.6
97.	Marius M	54.9W	17.3N	10.7
98.	Maskēlyne	30.0E	2.1N	6.3
99.	Menelaus	15.9E	16.2N	4.1
				5.1
100.	Mercator A	27.8W	30.6S	8.8
101.	Messier A	46.9E	2.0S	5.6
102.	Milichius	30.2W	10.0N	1.4
				9.8
				12.7
103.	Milichius A	32.0W	9.3N	12.5
104.	Moltke	24.2E	0.6S	5.8

	Feature	Location		Days After Sunset
105.	Newcomb	43.7E	29.8N	7.4
106.	Nicollet	12.4W	21.9S	10.1
				10.1
107.	Olbers A	77.6W	8.1N	8.8
108.	Opelt	17.5W	16.3S	12.9
				13.7
109.	Palisa P	7.3W	9.7S	13.7
110.	Pitatus	13.5W	29.8S	10.0
111.	Piton B	0.1W	39.3N	11.1
112.	Plinius	23:6E	15.3N	2.7
				5.8
113.	Posidonius P	27.5E	33.3N	6.1
114.	Posidonius	24.5E	30.0N	5.8
115.	Proclus	46.9E	16.1N	4.6
				6.7
				7.7
116.	Regiomontanus C	5.2W	28.8N	1.3
				10.7
				10.7
117.	Reiner	54.9W	6.9N	6.6
				7.8
				10.7
118.	Reiner A	51.4W	5.1N	8.1
119.	Reiner C	51.4W	3.5N	8.1
				11.0

	Feature	Location		Days After Sunset
120.	Reinhold	22.8W	3.3N	13.3
121.	Reinhold NA	25.4W	1.9N	1.8
				9.0
				13.1
122.	Romer	36.4E	25.4N	3.7
				5.8
				6.8
123.	Romer L	34.7E	23.2N	3.6
				6.7
124.	Ross	21.7E	11.6N	4.6
				5.6
125.	Ross G	24.8E	10.6N	3.8
126.	Rutherfurd	12.1W	60.9S	10.1
127.	Suess	47.7W	4.4N	7.2
				8.4
				11.3
128.	Suess F	44.6W	1.1N	7.5
				11.5
129.	Tacquet C	21.0E	13.4N	5.6
130.	Thebit A	4.9W	21.6S	10.7
131.	Theophilus	26.3E	11.4S	13.2
132.	Tobias Mayer	26.0W	12.2N	13.0
133.	Torricelli	28.5E	4.7S	13.4
34.	Torricelli B	29.2E	2.6S	13.5

	Feature	Location		Days After Sunset
135.	Tralles A	47.0E	27.4N	4.6
				6.7
				7.7
136.	Triesnecker	3.6E	4.1N	4.1
				11.4
137.	Tycho	11.2W	43.2S	8.5
				10.2
138.	Vitello	37.5W	30.4S	8.0
				8.0
139.	Vitruvius A	33.8E	17.7N	5.6
				6.6
140.	Vitruvius C	33.9E	15.3N	6.6
141.	Werner D	3.0E	27.0S	11.3
142.	Zuchius	50.9W	61.5S	6.9
143.	3E 14N			3
				4
144.	10E 12N			4
145.	11E 20N			5
146.	25E 30N			6
				14.3
147.	60E 34N			9
148.	69E 24N			8
				9
149.	43W 7N			9
				12

	Feature	Location	Days After Sunset
150.	13W 26S		10
151.	45W 24S		7
152.	50W 31S		7
153.	65W 27S		10

16. APPENDIX B

Positional Information on Eastern Edge of Nonlinear Cooling Region (Waning Moon)

A. Observation Set for May 20, 1968

Longitude of sunset terminator = 8.9W

Scan No.	Position of Eastern Edge	Days after Local Sunset
3	~38.2E 26.0N (Romer on edge)	~3.9
4	~36.1E 23.4N (Romer L on edge)	~3.7
7	35.6E 19.7N	3.7
9	36.3E 19.0N	3.7
10	35.0E 17.4N	3.6
12	35.4E 13.3N	3.6
13	33.0E 12.0N	3.4

B. Observation Set of May 21, 1968

Longitude of sunset terminator = 21.2W

Scan No.	Position of Eastern Edge	Days after Local Sunset
3	22.9E 9.8N	3.6
4	21.8E 8.2N	3.5
5	20.6E 6.6N	3.4
7	21.4E 5.6N	3.5
8	~20.3E 4.0N (Dionysius on edge)	>3.4
9	21.3E 3.4N	3.5
10	22.4E 2.3N	3.6
11	21.2E 0.7N	3.5

B. Observation Set of May 21, 1968

Longitude of sunset terminator = 21.2W (Continued)

Scan No.	Position of Eastern Edge	Days after Local Sunset
12	21.1E 0.6S	3.5
13	22.1E 1.4S	3.6
15	17.2E 5.8S	3.2
16	21.8E 5.3S	3.5

Longitude of sunset terminator = 22.2W

Scan No.	Position of Eastern Edge	Days after Local Sunset
2	20.6E 11.0S	3.5
3	20.0E 12.5S	3.5
4	20.5E 13.6S	3.5
6	22.9E 15.3S (poorly defined limb deflection)	3.7
7	23.3E 16.5S	3.7
9	25.4E 19.5S	3.9
10	26.6E 20.8S	4.0

C. Observation Set of March 24, 1968

Longitude of sunset terminator = 34.5W

Scan No.	Position of Eastern Edge	Day after Local Sunset
7	~11.7E 20.0N (Feature on edge)	~3.8
8	12.9E 18.5N	3.9
9	15.0E 17.3N	4.1
10	11.1E 14.5N	3.7
11	8.3E 11.9N (Anomaly on edge)	3.5

C. Observation Set of March 24, 1968

Longitude of sunset terminator = 34.5W (Continued)

Scan No.	Position of Eastern Edge	Day after Local Sunset
12	10.4E 10.1N	3.7
13	10.3E 8.3N	3.7
14	10.0E 6.7N (Anomaly on edge)	3.7

D. Observation Set of May 23, 1968

Longitude of sunset terminator = 46.4W

Scan No.	Position of Eastern Edge	Days after Local Sunset
3	~8.1E 26.4N (Feature on edge)	~4.5
4	~8.5E 25.9N (Feature on edge)	~4.5
5	~9.6E 24.6N (Feature on edge)	~4.6
6	~7.2E 23.1N (Feature on edge)	~4.4
7	8.7E 22.6N	4.5
10	6.1E 17.5N	4.3
11	7.6E 16.8N (Feature on edge)	4.4
12	9.0E 16.1N	4.5
14	3.8E 11.9N	4.1
15	9.3E 13.3N	4.6
20	8.4E 11.8N (Feature on edge)	4.5
21	8.8E 11.0N	4.5
22	3.7E 8.2N	4.1
23	3.1E 7.0N	4.1
24	2.5E 5.9N	4.0
25	2.7E 5.1N	4.0

D. Observation Set of May 23, 1968

Longitude of sunset terminator = 46.4W (Continued)

Scan No.	Position of Eastern Edge			Days after Local Sunset
26	1.1W	2.5N		3.7
27	4.7E	3.7N	(Indistinct transition)	4.2
28	0.1E	9.8N		3.8
29	~0.7E	0.4N	(Feature on edge)	~3.9
30	2.0E	0.4S		4.0
31	0.9E	1.4S		3.9

Longitude of sunset terminator = 47.4W

Scan No.	Position on Eastern Edge			Days after Local Sunset
36	0.8E	1.5S		4.0
37	1.7E	1.8S	(Feature on edge)	4.0
38	0.1W	3.6S		3.9
39	0.8E	3.9S		4.0
40	0.3E	4.7S		3.9
42	0.8E	6.4S		4.0
7	1.3E	8.6S		4.0
11	2.6E	10.9S	(Feature on edge)	4.1
12	3.1E	11.4S		4.1
18	6.0E	15.6S		4.4
19	6.4E	16.4S		4.4

17. REFERENCES

Adams, John B., and Robert L. Jones, Spectral Reflectivity of Lunar Samples, Science, 167, 737, 1970.

Allen, D. A., and E. P. Ney, Lunar Thermal Anomalies: Infrared Observations, Science, 164, 419, 1969.

Armstrong, Ken, Infrared Radiometry of the Planets, Masters Thesis, Space Science Dept., Rice University, 1971.

Ashby, Neil, Energy Balance on the Lunar Surface, Publ. of the Astron. Soc. of the Pacific, 78, 254, 1966.

Carslaw, H. S., and J. C. Jaeger, Conduction of Heat in Solids, Oxford University Press, 1959.

Dicke, R. H., and R. Beringer, Microwave Radiation from the Sun and Moon, Astrophys. J., 103, 375, 1946.

Geoffrion, Ann R., Majorie Korner, and William M. Sinton, Isothermal Contours of the Moon, Lowell Observatory Bull., 5, 1, 1960.

Jaeger, J. C., and A. F. A. Harper, Nature of the Surface of the Moon, Nature, 166, 1026, 1950.

Jaeger, J. C., The Surface Temperature of the Moon, Australian Jour. of Physics, 6, 10, 1953.

Krotikov, V. D., and O. B. Shchuko, The Heat Balance of the Lunar Surface Layer During a Lunation, Soviet Astron. - AJ, 7, 228, 1963 (English Translation)

Linsky, Jeffrey L., Models of the Lunar Surface Including Temperature-Dependent Thermal Properties, Harvard College Observatory Scientific Report No. 8, 1966.

Low, Frank J., Low-Temperature Germanium Bolometer, J. O. S. A., 51, 1300, 1961.

Low, Frank J., Lunar Observations at λ 10μ and 1.2 mm., Astron. J., 69, 143, 1964.

Low, Frank J., Lunar Nighttime Temperatures Measured at 20 Microns, Astrophys. J., 142, 806, 1965.

Low, F. J., Thermal Detection Radiometry at Short Millimeter Wavelengths, Proc. IEEE, 54, 477, 1966.

Low, F. J., and W. W. Mendell, Lunar Infrared Flux Measurements at 22 Microns, paper presented at the Planetary Subgroup of the American Astronomical Society, Austin, Texas, December, 1968.

Maxwell, A. D., Correction of the Variation per Hour of the Moon's Declination for Rate of Change of Parallox and Refraction of the Moon, Publ. of the Observatory of the Univ. of Mich, 4, 66, 1931.

McCord, Thomas B., Color Differences on the Lunar Surface, J. Geophys. Res., 74, 3131, 1969.

Mendell, W. W., and F. J. Low, Low-Resolution Differential Drift Scans of the Moon at 22 Microns, J. Geophys. Res., 75, 3319, 1970.

Murray, Bruce C., and Robert L. Wildey, Surface Temperature Variations During the Lunar Nighttime, Astrophys. J., 139, 734, 1964.

Pearse, C. A., Photometry and Polarimetry of the Moon and Their Relationship to Physical Properties of the Lunar Surface, Bellcomm Technical Report, TR-63-211-6, August 23, 1963.

Pettit, Edison, and Seth B. Nicholson, Lunar Radiation and Temperatures, Astrophys. J., 71, 102, 1930.

Pettit, Edison, Lunar Radiation as Related to Phase, Astrophys. J., 81, 17, 1935.

Pettit, Edison, Radiation Measurements on the Eclipsed Moon, Astrophys. J., 91, 408, 1940.

Pettit, Edison, The Co-Albedo of the Moon, Astrophys. J. 102, 14, 1945.

Piddington, J. H., and H. C. Minnett, Microwave Thermal Radiation from the Moon, Australian J. Sci. Res., A2, 63, 1949.

Roelof, Edmund C., Thermal Behavior of Rocks on the Lunar Surface, Icarus, 8, 138, 1968.

Rosse, Laurence (Earl of), On the Radiation of Heat from the Moon, Proc. Roy. Soc. London, 17, 436, 1869.

Saari, John M., and Richard W. Shorthill, Infrared Mapping of Lunar Craters During the Full Moon and the Total Eclipse of September 5, 1960, Boeing Sci. Res. Lab. DI-82-0176, July, 1962.

Saari, J. M., The Surface Temperature of the Antisolar Point of the Moon, Icarus, 3, 161, 1964.

Saari, J. M., and R. W. Shorthill, Isothermal and Isophotic Atlas of the Moon, NASA CR-855, September, 1967.

Shorthill, R. W., H. C. Borough, and J. M. Conley, Enhanced Lunar Thermal Radiation During a Lunar Eclipse, Publ. Astron. Soc. of the Pacific, 72, 481, 1960.

Shorthill, R. W., and J. M. Saari, Lunar Infrared Temperature Measurements During September 4, 5, & 6, 1960. Boeing Airplane Co. Doct. D7-2550-1, January, 1960.

Shorthill, Richard W., Measurements of Lunar Temperature Variations During an Eclipse and Throughout a Lunation, Boeing Sci. Res. Lab. DI-82-0196, August, 1962.

Shorthill, Richard W., and John M. Saari, Radiometric and Photometric Mapping of the Moon Through a Lunation, Annals of the New York Acad. Sci., 123, 722, 1965.

Shorthill, R. W. and J. M. Saari, Infrared Observation on the Eclipsed Moon, Boeing Sci. Res. Lab. Doct. DI-82-0778, January, 1969.

Sinton, William M., Observations of Solar and Lunar Radiation at 1.5 Millimeters, JOSA, 45, 975, 1955.

Sinton, William M., Observation of a Lunar Eclipse at 1.5 mm., Astrophys. J. 123, 325, 1956.

Sinton, William M., A Pyrometer for Planetary Temperature Measurements, Lowell Observatory Bull., 4, 260, 1959.

Sinton, William M., Eclipse Temperatures of the Lunar Crater Tycho, in The Moon, edited by Z. Kopal and Z. K. Mikhailov, p. 469, Academic Press, New York and London, 1962.

Troitskii, V. C., On a Theory of the Radioemission of the Moon (in Russian), Astronomicheskii Zhurnal, 31, 511, 1954.

Wattson, Richard B., and Robert E. Danielson, The Infrared Spectrum of the Moon, Astrophys. J., 142, 16, 1965.

Weaver, Harold, The Interpretation of Thermal Emission from the Moon, in Solar System Radio Astronomy: NATO Advanced Study Institute of the National Observatory of Athens, Cape Sounion, Greece, August 2-15, 1964, lectures, p. 295, edited by Jules Aarons, Ionospheric Institute of the National Observatory, Athens, 1965.

Wesselink, A. J., Heat Conductivity and Nature of the Lunar Surface Material, Bull. Astron. Inst. of the Netherlands, 10, 351, 1948.

Wildey, Robert L., Bruce C. Murray, and James A. Westphal, Reconnaissance of Infrared Emission from the Lunar Nighttime Surface, J. Geophys. Res., 72, 3743, 1967.

Wildey, Robert L., The Nocturnal Heat Sources of the Surface of the Moon, Mon. Not. Royal Astron. Soc., 139, 471, 1968.

Winter, D. F., and J. M. Saari, A Particulate Thermophysical Model of the Lunar Soil, Astrophys. J., 156, 1135, 1969.